Experimental Comparison of Two MRI-Compatible Flow Olfactometer Architectures

by

Tom P. Nielen

In partial fulfilment of the requirements for the degree of
Master of Science
at Delft University of Technology,
to be defended publicly on 15-7-2025.

Faculty: Mechanical Engineering
Department: Cognitive Robotics
Programme: MSc Mechanical Engineering: BioMechanical Design
Student nr: 4905865

Mentors / Supervisors: A.L. Ratschat
Dr. L. Marchal Crespo
Dr. J. Zimmermann
Graduation committee: A.L. Ratschat
Dr. L. Marchal Crespo
Dr. T. Horeman

TU Delft

Experimental Comparison of Two MRI-Compatible Flow Olfactometer Architectures

Tom P. Nielen – 4905865
Supervisors: A.L. Ratschat, Dr. L. Marchal Crespo, and Dr. J. Zimmermann

***Abstract*—Olfactory research shows a link between olfaction and neurodegenerative diseases, such as Alzheimer's and Parkinson's. To study these neural mechanisms, functional Magnetic Resonance Imaging (fMRI) together with flow olfactometry is employed. This study evaluated two MRI-compatible flow olfactometer architectures; the classic air-dilution Lorig layout and a continuous flow vacuum-switch architecture, both built from the same modular base hardware. Both systems were benchmarked head-to-head under identical MRI constraints. Key performance metrics included temporal stimulus precision, stimulus shape, achievable odor vapor concentration range, cross-contamination, airflow stability at the participant interface and MRI compatibility. Air carrier flow rate was varied between $1-10\,\mathrm{L\,min^{-1}}$, delivery tube length between $1-9\,\mathrm{m}$, and air dilution ratios between $2.5-90\,\%$. For the concentration measurements, undiluted isoamyl acetate was used in combination with a photo-ionization detector. The results show that the vacuum-switch cut stimulus onset latency by $35-60\,\%$ and kept it below $500\,\mathrm{ms}$ with $9\,\mathrm{m}$ tubing, producing the flattest square stimulus pulses and reducing residual odor to below $1.6\,\%$ of the primary response. These gains came at the cost of brief flow rate dips of approximately $70\,\%$ below target during valve transitions and a $20-35\,\%$ lower maximum odor vapor concentration. The Lorig system delivered higher peaks and steadier flow but showed longer, tube length dependent latency and stronger cross-contamination of approximately $4\,\%$. Neither configuration reduced temporal signal-to-noise ratio (tSNR) for fMRI measurements. Together, the results provide quantitative trade-offs that allow researchers to match olfactometer design to the specific timing, intensity and comfort requirements of future olfactory fMRI studies, ultimately assisting research in uncovering the underlying neural mechanisms of human olfaction.**

I. Introduction

OLFACTORY research has emerged as a major research subject related to neurodegenerative diseases, including Alzheimer's disease, idiopathic Parkinson's disease, and multiple sclerosis [1]. In the case of Alzheimer's, for instance, changes in olfactory function are known to precede the onset of cognitive or motor symptoms by years [2], [3]. More recently, a less studied phenomenon, the loss or change of smell in stroke patients, has gained attention [4], [5]. However, this phenomenon has yet to be investigated with high spatial resolution techniques such as functional magnetic resonance imaging (fMRI). Understanding the neural mechanisms underlying olfactory processing presents an opportunity for earlier diagnosis and, potentially, therapeutic intervention. fMRI is particularly well suited to this line of research: it is non-invasive, repeatable, and offers high spatial resolution alongside temporal resolution sufficient for event-related studies, enabling researchers to monitor brain activity within the timeframe of a single sniff. This is essential since humans are generally capable of identifying an odor with one sniff [6]. Precise, well-timed delivery of odor stimuli inside the MRI bore, however, is technically challenging. Magnetic field constraints prohibit the use of ferrous or electronic components near the bore, and due to the cavities located near the olfactory bulb, even a small increase in noise can confound signal interpretation [1].

To meet these challenges, an MRI-compatible flow olfactometer must fulfill a set of demanding design requirements that ensure precise, reliable, and artifact-free odor delivery within the MRI environment. First, stimulus latency and shape are critical. The onset and offset of an odor pulse should be steep and resemble a square wave to ensure that neural responses can be attributed to the periods of stimulation. However, long tubing and low flow rates can degrade this shape and increase onset delay due to diffusion and adsorption effects [7]. Second, precise concentration control is essential. Since perceived odor intensity follows a logarithmic psychophysical relationship known as Weber's law [8], the system must be capable of delivering accurate and repeatable intensities across a broad range of concentrations. This is typically achieved through the use of air dilution with mass flow controllers (MFCs) or liquid dilution. Third, the system must prevent cross-contamination and avoid providing non-olfactory cues. Switching between odorized and clean air must occur seamlessly, without introducing thermal or tactile sensations and without residual odor from previous stimuli. This requires the use of non-adsorptive materials, like polytetrafluoroethylene (PTFE), and a constant airflow design. Lastly, MRI compatibility imposes strict constraints on materials, particularly for components located within the Faraday cage or near the scanner bore, where ferromagnetic materials are prohibited.

These design considerations are often interdependent. For example, reducing tubing length to improve latency may require placing odor reservoirs inside the scanner room, which introduces challenges related to MRI safety and signal integrity. On the other hand, situating all components outside the MRI room simplifies MRI compatibility but can degrade temporal precision and the stimulus shape. As a result, a variety of design approaches have been proposed. Some employ an odor injection-based system, in which odorant is directly injected into a constant airflow [9]. Others place odorant canisters within the MRI room or even inside the MRI bore to reduce the distance between the odor source and the subject [10]. In this study, two designs that are widely used in the field were selected for evaluation. The vacuum-assisted, continuous-flow

architecture [11] offers low latency but involves more complex plumbing and calibration. In contrast, the Lorig-style design, named after its originator [12], relies on MFC networks for odor delivery and is simpler to construct and scale. However, it tends to produce longer latencies and degraded stimulus shapes, particularly when the delivery line exceeds several meters in length. Both designs share a common method of odor generation and selection, in which airflow is odorized by passing through a canister outside of the MRI room containing the liquid odorant. To date, no study has benchmarked these two approaches head-to-head under identical MRI constraints. This leads to the following research question: *How do two MRI-compatible flow olfactometer designs – a Lorig-style and a vacuum-switch architecture – compare in terms of temporal precision, stimulus shape, stimulus intensity, cross-contamination, and non-olfactory stimulation?*

To address this question, both configurations were evaluated experimentally across a range of conditions representative of practical fMRI use. In addition to directly comparing the two architectures, the influence of key system parameters, including delivery tube length, carrier flow rate, and dilution ratio, were systematically investigated. By benchmarking these configurations and variables against the performance criteria, this work provides evidence-based guidelines for designing high-performance olfactometers for fMRI studies, supporting more reliable olfactory neuroimaging and advancing our understanding of the neural mechanisms of olfaction.

II. Materials and Methods

To address the research question effectively, a robust and versatile olfactometer setup that can be configured to implement both the Lorig-style and vacuum-assisted designs is essential. This section outlines the rationale behind the design decisions, details the components used in the construction of the system, and describes the measurement methods employed for evaluating olfactometer performance.

A. Olfactometer design

Flow olfactometers can be broken down into three primary subsystems [11], [13]. The first subsystem is the carrier gas preparation system, which provides the carrier gas, often air, and prepares it by removing any existing contaminants or odors. The second subsystem handles the odorant selection by routing the airflow through the specified odorant canister and controls the concentration by mixing the odorized air with odorless control air. The final subsystem describes the delivery method, which directs the odorized air to the subject's nose. The key distinction between different olfactometer architectures lies in how the mixing and delivery of airflow are managed. Up to the point of odor selection, both the Lorig-style and vacuum-assisted configurations share identical components and structure.

1) Lorig-style configuration: The Lorig-style configuration serves as the baseline system upon which the vacuum-assisted design is later built. The working principle is simple, which makes it a popular design choice for olfactory studies in general [14], [15], [16], [17]. As illustrated in Fig. 1a, the setup starts with a pressurized air supply, which is passed through an activated carbon filter to eliminate existing odors and contaminants. The airflow is then divided into two branches: the odor line and the dilution line. Each branch is regulated using mass flow controllers (MFCs), allowing for precise, flow-based control rather than relying on pressure differentials, which is essential for generating a constant flow rate. The odor line is directed into a splitting manifold, which distributes the airflow into individual channels, each connected to a separate odorant canister. The selection of a specific odorant is controlled via normally closed solenoid valves. The airflow is then odorized as it passes through the selected odorant canister. To reduce backflow and cross-contamination, check valves are installed immediately downstream of the odorant reservoirs. After odorization, the odor line is recombined with the dilution line in a mixing manifold, enabling controlled dilution of the stimulus. The resulting mixture is then delivered through the Faraday cage into the MRI room via the stimulus line. In this configuration, the transition between stimulus and no-stimulus states is achieved by adjusting the relative flow rates of the two MFCs; for instance, setting the dilution MFC 1 to 100 % effectively bypasses odor delivery.

2) Vacuum-switch configuration: The vacuum-switch configuration builds upon the same infrastructure as the Lorig-style setup but introduces a modified delivery mechanism. As shown in Fig. 1b; the key difference lies in how the final switching between odorous and clean air is performed. Originally introduced by Kobal [18] and later adopted in several olfactometer designs [11], [19], this approach shifts the switching point from the olfactometer itself to the end of the delivery line, closer to the subject. Rather than relying solely on MFCs for stimulus control, this design incorporates a switching mechanism with vacuum lines located inside the MRI bore. In this arrangement, both the stimulus line (carrying odorized air) and a control line (carrying clean air) are routed into the MRI room. A 3-way valve, positioned outside of the MRI room, connects to two vacuum lines, each attached to one of the air lines. When the vacuum is applied to one line, the corresponding airflow is diverted away, allowing the other to be delivered to the subject. Switching the 3-way valve redirects the vacuum to the opposite line, thereby changing which airflow reaches the subject. By moving the switching mechanism closer to the participant, this configuration enables rapid transitions between odorized and clean air, theoretically resulting in improved temporal precision and stimulus shape quality.

B. Components

The olfactometer system is composed of a variety of components, which can broadly be categorized as either odorant-specific or non-odorant-specific based on their exposure to odorized air. Odorant-specific components are those that come into direct contact with the odorant and are therefore susceptible to contamination. As long as the same odorant is used consistently across repeated measurements, contamination within these components is manageable. However, if the odorant is changed, thorough cleaning or replacement is

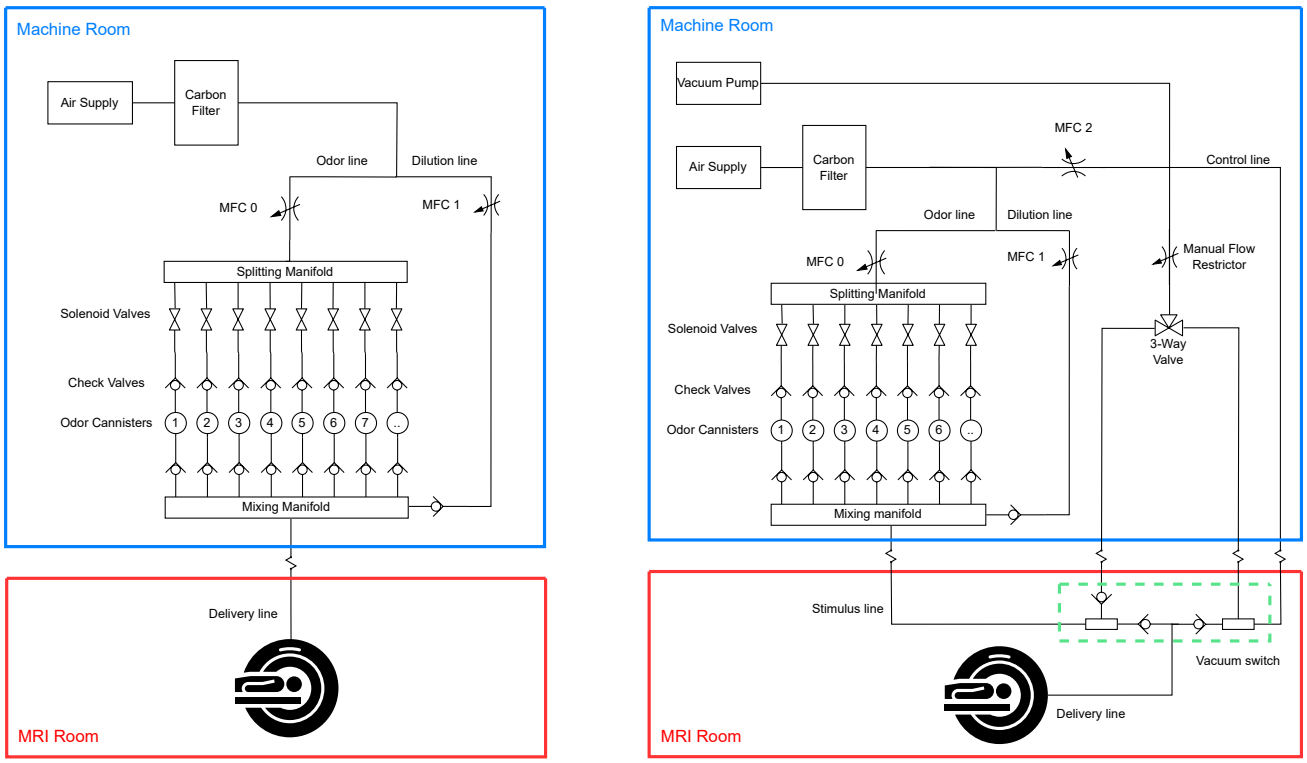

(a) Lorig-style configuration. The length of the delivery line is not to scale.

(b) Vacuum-switch configuration. The green dotted box shows the pneumatic diagram for the vacuum-switch.

Fig. 1: Air flow diagrams for both configurations. All individual components are annotated. The blue box describes the machine room outside of the MRI Faraday cage, and the red box inside the Faraday cage.

required to prevent cross-contamination. For instance, when reusing an odorant canister for a different substance, all glass elements must be carefully cleaned, and any rubber seal or O-rings should be replaced. In contrast, non-odorant-specific components, such as the mixing manifold and vacuum-switch, are designed to accommodate multiple odorants and are constructed from materials that resist odor adherence. Although these parts are less susceptible to contamination, routine maintenance and periodic cleaning remain necessary to ensure consistent performance and to avoid the accumulation of residual compounds over time. A detailed overview of all components is provided in the next section, and the full bill of material is listed in Appendix A.

1) Air supply: The system is supplied with compressed air at a pressure between 2.0 – 2.5 bar from a central air supply. The incoming air is first filtered through an activated carbon filter (MS4-LFX-1/4-R, Festo, Germany) to remove residual contaminants and odors. In some olfactometer designs, the air is also humidified and heated [11]. This can be advantageous, particularly in configurations using nasal cannulae for direct airflow delivery to the nostrils. In such cases, high humidity and temperature help to prevent nasal drying and discomfort during prolonged stimulation [20]. In the current design, however, odor delivery is achieved via an oxygen mask or an open-air canopy rather than nasal cannulae. As a result, the need for humidification and heating is reduced, and higher airflow rates can be utilized without compromising subject comfort [21].

2) Tubing & Fittings: Two types of tubing are used throughout the olfactometer system, selected based on their material properties and exposure to odorized air. An important design consideration is minimizing odor adherence to internal surfaces, as this can degrade stimulus quality and contribute to cross-contamination. For this reason, polytetrafluoroethylene (PTFE) tubing (6 × 4 mm, Landefeld, Germany) is utilized in all sections of the device that come into contact with odorized air. PTFE offers excellent chemical resistance and minimizes the adsorption of volatile compounds to the tubing walls. It is also relatively easy to clean when contamination does occur due to the chemical resistance. However, PTFE's rigidity and higher cost make it less suitable for general-purpose routing. For sections of the device that do not carry odorized air, cheaper and flexible polyurethane (PU) tubing (PUN-H-6X1-NT, Festo, Germany) is used. This clear tubing is easy to handle and install, but it suffers from high odor adherence. As a result, any PU tubing that becomes contaminated should be discarded and replaced rather than cleaned. To further reduce the risk of odor carryover, all components downstream of the odorant canisters are non-odorant-specific and should thus be constructed from PTFE wherever feasible. The mixing manifold is a critical junction in the system and is constructed from a block with 18 inlet/outlet ports (Manifold-18 Outlets-1/8" BSPF, TU-LOK, India). Connections to the tubing are fittings also made from PTFE (Male 6 mm OD × 1/8" BSPM, TU-LOK, India), ensuring tight seals to the PTFE tubing.

3) Odorant canisters: The odorant canisters, as seen in Fig. 2, are constructed from 100 mL glass gas washing bottles (100 mL-PP, LaborXing, China), and are classified as odorant-specific. These bottles are sealed using rubber washers and O-rings to make them airtight. A custom 3D-printed connector, fabricated from polylactic acid (PLA), is used to mount standard steel push-in fittings (QSM-M7-6-I, Festo, Germany), making the canisters compatible with the PTFE tubing.

Various methods can be used to diffuse odor vapor into the air stream. Common methods include using solid odorants [22] or adding liquid odorant to a porous substance like felt [23] or cotton wads [24]. For this study, however, just liquid odorant is used, since most odorants come as liquid and it is more straightforward to maintain a static liquid-to-air surface area compared to the porous substance method. To control the evaporation rate, odorants are diluted in either light mineral oil or propylene glycol, both common solvents for olfactory studies [25], with the choice of solvent dependent on the solubility of the odorant chemical in each solvent. Each canister contains a total amount of 20 mL of liquid, ensuring that the bottom of the bottle is fully covered. This maintains a consistent liquid-to-air surface area. The inner glass tube of the gas washing bottle cap is placed approximately 1 cm above the surface of the liquid. The tube is not placed in the liquid to prevent excessive agitation of the liquid, which might generate droplets that could contaminate the tubing down the line [21].

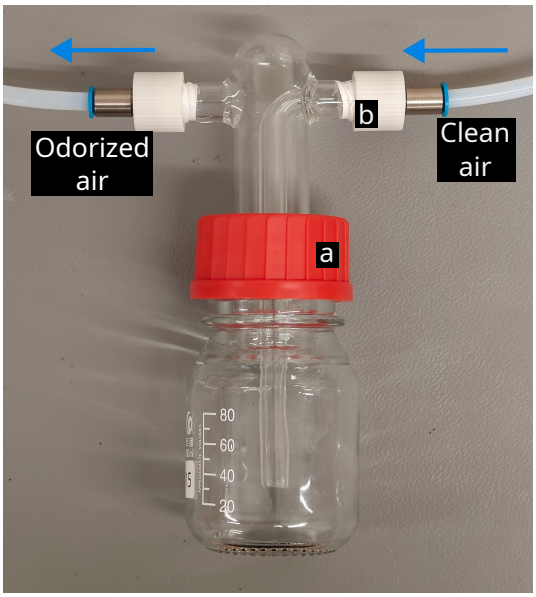

Fig. 2: Odorant canister without any odorant. Rubber seal rings are used in the red cap (a) and the white 3D-printed parts (b). The bottle is connected to two PTFE tubes; one is the clean intake air and the other the odorized air.

4) Solenoid Valves: Odorant selection is controlled using fast-switching solenoid valves (MHP2-M1H-3/2G-M5, Festo, Germany), which are mounted onto interconnected aluminum manifold blocks (MHP2-PR8-3, Festo, Germany). These manifolds divide the incoming odorized airflow into independent channels, each corresponding to a specific odorant. The valves operate in a 3/2 normally closed configuration, meaning that when the valve is de-energized, the input flow is redirected rather than completely blocked. While this configuration is useful in general pneumatic applications, it introduces the possibility of backflow between channels in the context of odorant selection. To mitigate this risk and ensure isolation between odorant lines, the unused outlet port of each valve is sealed at the manifold level. This modification effectively converts the valves to behave as 2/2 normally closed valves, allowing airflow only when the corresponding valve is actuated and reducing the amount of cross-channel contamination during switching.

5) Mass Flow Controllers: To generate a consistent airflow, a combination of three mass flow controllers (MFC) is used. These devices maintain a consistent flow rate, provided that sufficient inlet pressure is maintained. In the Lorig-style configuration, two MFCs (SFC6000D-20SLM, Sensirion, Switzerland) are used, one to regulate the odorized air line and another for the dilution line. In the vacuum-assisted configuration, an additional MFC is required to drive the control line, which manages the vacuum-switch mechanism. For this purpose, a higher-capacity MFC (SFC6000D-50SLM, Sensirion, Switzerland) is used. The flow rate of the control line must equal the combined flow rates of the odor and dilution lines to maintain a constant total flow and reduce flow fluctuations during stimulus transitions. Thus, the theoretical maximum flow rate of the system is $40\,\mathrm{L\,min^{-1}}$ with a dilution ratio of 50 %.

6) Check Valves: Check valves (Check valve 6×6 mm, TU-LOK, India) are incorporated throughout the olfactometer to maintain a consistent unidirectional airflow and to minimize the risk of backflow and cross-contamination between odorant channels. Their most critical placement is immediately downstream of the odorant canisters, where odorized air reenters the shared flow path. These valves are primarily composed of PTFE to ensure chemical inertness and low odor adherence. However, an internal rubber seal ring and a steel spring are essential for valve function, which introduces odorant-specific elements that may retain some odor. As a result, each check valve placed after the odorant canisters is considered odorant-specific and must consistently be used with the same odorant during repeated trials. When an odorant channel is repurposed for a different substance, the associated check valves must be fully disassembled and cleaned. Due to the potential for persistent odor retention in the rubber components, the seal rings should be replaced.

7) Vacuum-switch: The vacuum-switch assembly, shown in Fig. 3, is based on the design from Johnson and Sobel [11]. It consists of three PTFE tee unions (Union Tee $6 \times 6 \times 6$ mm, TU-LOK, India) and three PTFE check valves, which are identical to those used in the odorant selection module. The assembly is mounted to the MRI bed with two custom 3D-printed PLA brackets. The manifold features two positive pressure inlets: one PU tube supplies clean air, and one PTFE tube supplies the stimulus air, along with two corresponding PU vacuum tubes. The vacuum is provided by a vacuum piston pump (VP750-30L, VacuumChambers.eu, Poland) capable of drawing $120\,\mathrm{L\,min^{-1}}$ of air. A 3-way valve (MHE3-M1H-3/2G-1/8-K, Festo, Germany), located outside the MRI room and connected to the vacuum pump, controls which inlet flow is diverted. When the vacuum is applied to the control line,

clean air is evacuated, and the odorized stimulus reaches the subject. When the vacuum is switched to the stimulus line, the stimulus air is removed, and clean air is delivered instead. A check valve in the stimulus vacuum line prevents any backflow of odor into the stimulus line.

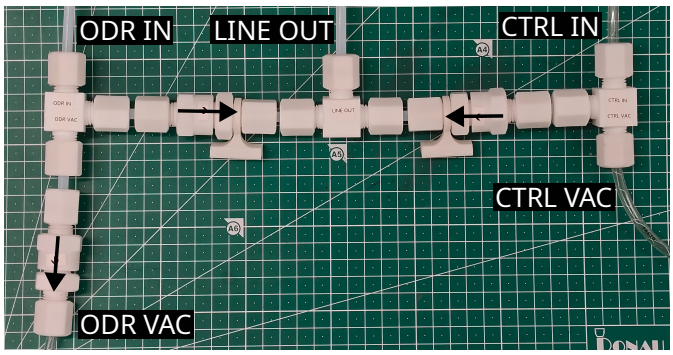

Fig. 3: Vacuum-switch based on Johnson and Sobel's design. (ODR IN) stimulus air line, (CTRL IN) control air line, (ODR VAC) stimulus vacuum line, (CTRL VAC) control vacuum line, (LINE OUT) delivery line to the subject. Arrows show the flow direction of the check valves.

8) Delivery apparatus: A conventional method for odor delivery involves the use of nasal cannulae, small tubes inserted directly into the subject's nostrils [10]. While this approach allows for direct and localized odor presentation, it often compromises participant comfort, especially at higher flow rates or under low humidity conditions. Such conditions may lead to nasal irritation or drying over the course of an experiment. To mitigate these issues, two alternative delivery methods were explored: a face mask, which is also conventional in flow olfactometry [17], and a free-standing tube. The face mask used is a standard oxygen mask (EcoLite, LungenLiga, Switzerland), featuring a single inlet perpendicular to the face and side openings for exhalation. This setup enables consistent delivery while allowing exhaled air to exit the system passively, reducing odor buildup within the mask.

The free tube method is less conventional, but it eliminates the need for a mask altogether. In this configuration, a delivery tube is mounted to the MRI head coil and positioned approximately 10 cm from the subject's nose at a downward angle of 5°. This setup provides a non-invasive and comfortable experience for the participant. To prevent odor accumulation around the bore, a vacuum hood positioned above the subject can be used, following the odor canopy design introduced by Gorodisky [26].

9) Housing and mounting: The final olfactometer system was constructed using a modular two-compartment design, housed in two aluminum cases (Classic 48, Alutec, Germany), as shown in Fig. 4. The lower compartment contains all essential electronic and control components, the main air intake with an activated carbon filter, and the three MFCs. From this compartment, each regulated air line is routed laterally to the upper compartment via PU tubing. The upper compartment is dedicated to odorant selection and mixing. It houses 16 odorant canisters, each connected to its corresponding solenoid valve, as well as check valves and the mixing manifold. This upper module is also the origin point for the four outlet tubes: the two air streams and the vacuum lines for the vacuum-switch configuration. In the vacuum-switch setup, all four tubes are routed to the external switching unit. In the Lorig-style configuration, only the odor line is used; the remaining three lines remain disconnected. This two-box system was selected to facilitate ease of access and maintenance. The upper compartment can be opened independently, allowing for quick replacement or refilling of odorant canisters and basic system checks without disturbing the control electronics. The lower compartment remains closed during normal operation and only requires access for periodic replacement of the carbon filter or in the event of hardware failure.

10) Electronics and Software: The olfactometer is operated by a Raspberry Pi 4 Model B (RPi) running Ubuntu Server 22.04 with the Robot Operating System (ROS) 2 Humble. The RPi hosts all configuration-specific logic, coordinates actuation of valves and MFCs, and manages communication with the control PC. These tasks are organized into separate ROS nodes. A detailed diagram of the ROS nodes and topics for both configurations is provided in Appendix B. The key distinction between the two configurations lies in the main control node. This node communicates with the control PC, calculates the appropriate flow rates, and determines which valves should be actuated. All other nodes, which are responsible for communicating with the MFCs, actuating the valves, and collecting sensor data, remain unchanged between configurations.

The basic electrical diagram of the olfactometer setup is provided in Appendix C. The three MFCs are connected to the RPi via USB serial, allowing direct control and feedback over flow rates. Solenoid valves are actuated through an Arduino Mega2560, which receives simple text-based serial commands from the RPi over a separate USB connection. The Arduino controls the valves via two relay modules: a 16-channel (TC-9445344, Conrad, Germany) for the 16 odorant valves, and 4-channel (4-Channel Relay Module, Purecrea, Germany) for the 3-way solenoid valve. A dedicated Ethernet connection links the RPi to the control computer. During experiments, the control computer sends structured stimulus messages over HTTP containing the selected odorant (or clean air), the air-to-odor dilution ratio, the desired total flow rate, and the stimulus duration.

11) Control logic: The control logic differs between the Lorig and vacuum-switch configurations due to their distinct methods of stimulus delivery. In the Lorig configuration, switching between odorized and clean air is done by opening or closing the specific odorant valve and adjusting the flow rate setpoints of the mass flow controllers (MFCs). When no stimulus is required, the dilution MFC provides 100 % of the total airflow, while the odor MFC (MFC 0) remains inactive. Stimulus delivery is achieved by setting both MFCs to match the desired odor-to-air dilution ratio and opening the solenoid valve for the selected odorant channel.

The vacuum-switch configuration employs a more advanced control sequence, as the switching between odorized and clean air occurs at the vacuum-switch located inside the MRI bore. Because of the physical distance between the odorant canisters and the switch, the stimulus line must be preloaded to ensure that odorized air reaches the subject immediately

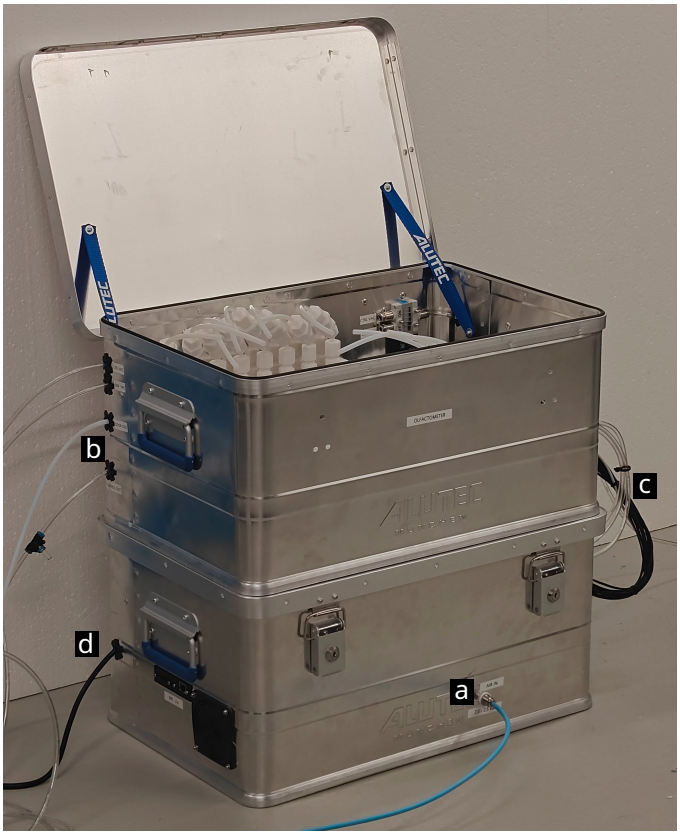

(i) Full olfactometer device in machine room. (a) air inlet, (b) four outlet tubes, (c) pneumatic and electric connection between the top and bottom compartment, (d) power cord.

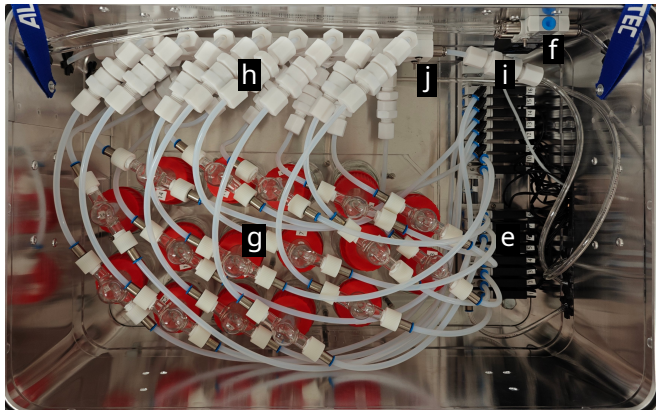

(ii) Top box. (e) solenoid valves, (f) 3-way valve, (g) odorant canisters, (h) check valves, (i) dilution line, (j) mixing manifold.

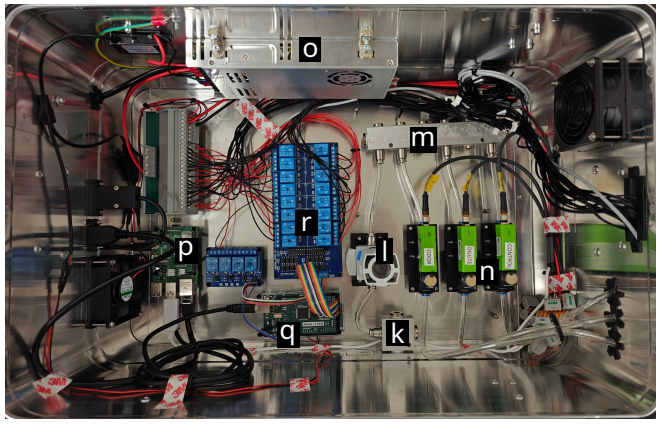

(iii) Bottom box. (k) air inlet, (l) activated carbon filter, (m) air flow splitter, (n) MFCs, (o) power supply unit, (p) Raspberry Pi, (q) Arduino Mega, (r) 16-channel relay module.

Fig. 4: Overview of the olfactometer system. (i) Fully assembled unit. (ii) Top box with odorant selection and dilution. (iii) Bottom box with electronics and air conditioning.

upon activation. To accomplish this, the stimulus line is flushed with odorized air for two seconds before switching. During this preload phase, the flow rate is temporarily boosted to $10\,\mathrm{L\,min^{-1}}$ while maintaining the desired dilution ratio. This elevated flow continues for 0.6 seconds after the 3-way valve is actuated. In addition, the vacuum pressure is restricted to $0.5-0.6\,\mathrm{bar}$ and a flow restrictor limits the vacuum draw to $10\,\mathrm{L\,min^{-1}}$ to match the delivery flow. Balancing these flows at the moment of switching follows the principle described by Johnson and Sobel [11], who recommended matching the delivery flow rate to the vacuum flow rate to reduce disturbances. After this initial phase, the total flow is boosted by 5 % of the target flow rate, with both the odor and dilution line flows scaled proportionally. This is to compensate for small leaks and ensure the actual flow rate is closer to the target. When switching back to clean air, the control line is also briefly boosted to $10\,\mathrm{L\,min^{-1}}$; however, this boost is not extended after the valve switch, as the smaller volume of the vacuum line makes it unnecessary. Together, these calibrations help reduce switching artifacts and produce smoother transitions between stimulus states. More details and a plot of the MFC flow rates is provided in Appendix D.

C. Measurements

To answer the research question, the following factors are characterized: Temporal precision, stimulus shape, stimulus intensity, cross-contamination, non-olfactory stimulation, and MRI-compatibility. In addition to a direct comparison between the Lorig-style and vacuum-switch configurations, further variations were introduced in flow rate, delivery tube length, and dilution ratio to provide a more comprehensive understanding of flow olfactometer performance under different conditions. Two primary measurement types were performed: flow rate measurement and gas concentration measurement. The flow rate was monitored using a flow sensor (SFM4300, Sensirion, Switzerland) connected to the RPi via USB serial. The sensor was placed directly at the outlet of the delivery tube, and data was sampled at 62.5 Hz. This setup allowed precise tracking of flow transitions and detection of any flow disturbances during stimulus switching.

Gas concentration measurements were conducted using a photoionization detector (PID), as is common in flow olfactometry [23], [27]. The PID detects volatile organic compounds (VOCs) by ionizing them with high-energy ultraviolet (UV) light emitted from a 10.6 eV lamp. If a compound's ionization potential (IP) is lower than the photon energy, it be-

comes ionized, which means it releases an electron and forms a positively charged ion. These ions create a current between two electrodes, producing an output signal proportional to the VOC concentration. Therefore, the sensor is non-specific, and only VOCs with an IP below 10.6 eV are detectable using this method. While not all odorants are VOCs, some are well-suited for PID detection. For these experiments, isoamyl acetate, which has a distinct banana odor and an IP of 9.7 eV, was selected as the test odorant. This compound provides a strong and mostly linear response within the lower part of the PID's operational range. For all experiments, a volume of 20 mL of 97 % isoamyl acetate was loaded into the first odorant canister.

The PID was positioned at a fixed distance of 20 mm from the outlet of the delivery tube and angled down by 5° to simulate the distance of a subject's nose in an oxygen mask, see Fig. 5. To prevent VOC buildup, the air was continuously extracted using a solder vacuum placed near the sensor. The PID outputs an analog signal, which was sampled by a Teensy 4.2 microcontroller. Data was collected at 10 kHz and down-sampled on the microcontroller to 500 Hz by averaging every 20 samples. The resulting values, along with corresponding timestamps from the Teensy, were transmitted to the RPi and stored using a dedicated ROS node. The raw analog output, ranging from 0 to 4095, exhibited high-frequency noise, which was attenuated using a fourth-order low-pass Butterworth filter with a 5 Hz cutoff. The 5 Hz cutoff was selected because the expected dynamics of the stimulus signal, given the stimulus durations and rise/decay characteristics of both the system and the PID sensor, occur well below this frequency. This ensures that relevant signal content is preserved while effectively suppressing high-frequency noise. After filtering, the signal was linearly scaled to millivolts, matching the 3.3 V reference of the Teensy.

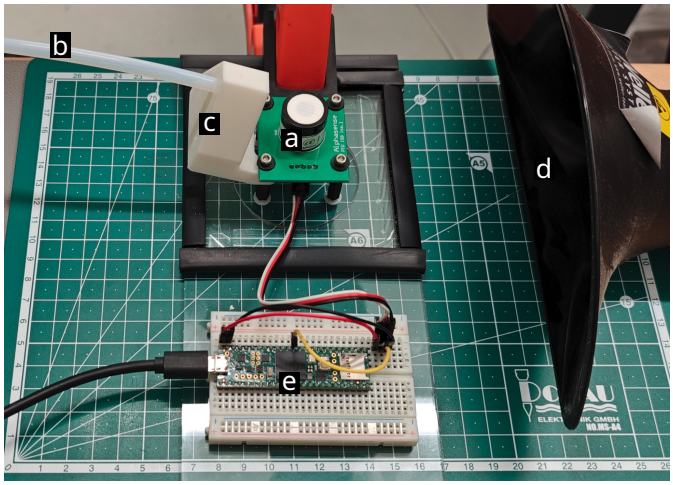

Fig. 5: PID test setup. (a) PID sensor, (b) stimulus tube, (c) 3D-printed tube mount, (d) vacuum, (e) Teensy 4.2.

1) Temporal precision: Temporal precision was assessed by measuring stimulus latency, defined as the time from valve actuation to the point at which the measured concentration reached 10 % of its peak value. In addition to comparing the Lorig and vacuum-switch configurations, two experimental variables were systematically varied: delivery line length and flow rate. Four tube lengths were selected to reflect different experimental scenarios. A 1-meter tube represents an unrealistic setup where the subject is positioned very close to the olfactometer. A 3-meter tube reflects behavioral testing distances, where no additional measurements are performed on the subject. A 6-meter length represents setups where the olfactometer is placed in a separate room to eliminate sensory cues. Finally, a 9-meter tube reflects the practical requirement for fMRI studies, spanning the distance between the machine room and the MRI bore. It should be noted that for the vacuum configuration, an additional meter of tubing is present between the vacuum-switch and the subject.

To evaluate the impact of flow rate on stimulus latency, five representative values were selected based on ranges commonly reported in the literature. Flow rates in existing olfactometer studies typically range from $0.5\,\mathrm{L\,min^{-1}}$ [14] to $10\,\mathrm{L\,min^{-1}}$ [28]. Within this range, the flow rates tested in this study were 1, 2, 4, 7 and $10\,\mathrm{L\,min^{-1}}$. Each combination of flow rate, tube length, and configuration was repeated ten times. For each condition, both the mean latency and the 95 % confidence interval were calculated to assess not only the average latency, but also the consistency of stimulus timing across repetitions. Confidence intervals were computed using the Student's t-distribution, based on the sample size of ten repetitions per condition.

2) Stimulus shape: To assess the quality and consistency of the odor stimulus, the temporal stimulus shape was evaluated using the PID. A well-formed stimulus should exhibit a rapid onset, stable plateau, and rapid offset, ideally forming a square pulse. To examine the influence of configuration, flow rate, and delivery tube length on stimulus degradation, the same variables used in the latency experiments were tested here. When delivery tube length was varied, the flow rate was fixed at $7\,\mathrm{L\,min^{-1}}$, a realistic value for comfortable and effective delivery. Conversely, when the flow rate was varied, the delivery tube was fixed at the full 9 m length required for fMRI setups. In each trial, a 10-second stimulus consisting of a 50:50 mixture of odorized and clean air was delivered to the PID. Each condition was repeated ten times, with a 2-minute flush between measurements to prevent carryover. The filtered PID voltage traces were averaged across measurements, and a 95 % confidence band was computed using the Student's t-distribution to visualize signal consistency and variability.

3) Stimulus intensity: An essential requirement of a well-performing olfactometer is the ability to regulate stimulus intensity. Therefore, characterizing how odorant concentration varies with the dilution ratio of clean to odorized air is critical for understanding and calibrating the system's behavior. To examine this relationship, a 30-second odor stimulus was delivered using both configurations at a fixed flow rate of $7\,\mathrm{L\,min^{-1}}$ and a tube length of 9 m; conditions that reflect typical fMRI use. The following dilution ratios, defined as the fraction of odorized air in the total flow, were tested: 2.5, 5.0, 7.5, 10, 15, 20, 25, 30, 40, 50, 60, 70, 80 and 90 %. A higher resolution was chosen at lower concentrations to better capture the expected non-linear relationship between dilution and measured signal. Each measurement was repeated five times, and between trials, the tubing was flushed for two

minutes to avoid contamination. To minimize the influence of initial rise time and system lag, the first 4 seconds of each PID trace were discarded. The mean PID voltage over the remaining 26 seconds was used as an indication for average odorant concentration. The 95% confidence interval of these five calculated means is also examined to test the repeatability of the achieved gas concentrations.

4) Cross-contamination: One of the main challenges in flow olfactometry is the prevention of cross-contamination, where residual odorant from a previous stimulus affects the delivery of subsequent stimuli or is detectable during supposed clean air periods. Cross-contamination can occur due to residual vapor within the tubing, valves, or mixing manifold and is especially problematic when stimuli are presented in rapid succession. To compare the susceptibility of the Lorig and vacuum-switch configurations to cross-contamination, a direct head-to-head test was conducted. In this test, three stimuli were delivered in sequence using three separate odorant canisters. The first canister contained isoamyl acetate (the detectable VOC), while the second and third were filled with light mineral oil, which should produce no PID signal. A 10-second stimulus was presented from each canister with a 10-second interval between stimuli. A flow rate of $7\,\mathrm{L\,min^{-1}}$ and a tube length of 9 m were used. For the dilution ratio, 90 % is chosen as a worst-case scenario for residual odors to accumulate. The measurement is repeated five times for both configurations. Cross-contamination was indicated by the presence of any secondary peaks in the PID signal during or after the second and third stimuli. The height of these peaks relative to the baseline and as a ratio of the primary peaks serves as a quantitative measure of contamination from the first odorant.

5) Non-olfactory stimulation: In olfactory experiments, it is essential to avoid non-olfactory cues that could influence the subject's perception. While visual and auditory cues are largely irrelevant inside the MRI bore, tactile cues resulting from sudden changes in airflow at the subject's face may still be perceptible and could introduce unwanted bias or anticipation. To evaluate this, the flow rate at the outlet of the delivery line was measured for both the Lorig and vacuum-switch configurations. The experiment involved a similar approach to the cross-contamination experiment, where three stimuli in sequence are presented, each separated by a 10-second interval of no stimulus. A flow rate of $7\,\mathrm{L\,min^{-1}}$ and a dilution ratio of 50 % were used for all trials, with the full 9 m delivery tube length to reflect typical fMRI usage. Flow was measured using the Sensirion flow sensor placed at the outlet, and each condition was repeated three times. The resulting flow traces were averaged to produce a representative profile for each configuration.

6) MRI Compatibility: To evaluate the MRI compatibility of the olfactometer, only the vacuum-switch configuration was tested, as this configuration has the highest risk of introducing noise due to the vacuum-switch. The Lorig setup only routes a single odor tube into the scanner. The test focused on whether the vacuum-switch introduced any measurable decrease in temporal signal-to-noise ratio (tSNR), which could indicate magnetic interference. Measurements were conducted using a spherical phantom positioned in a 32-channel head coil on a Philips 3T MRI scanner. The olfactometer was powered on, and a test program was run with a continuous flow rate of $7\,\mathrm{L\,min^{-1}}$ to ensure normal operation of the vacuum-switch, including switching of the check valves. Three conditions were tested: (1) the vacuum-switch placed directly next to the head coil inside the bore (worst case condition), (2) at the bore entrance near the subject's waist, and (3) outside the scanner room, serving as a control. The position was altered by sliding the vacuum-switch up and down the rails on the side of the MRI bed, see Fig. 6. Each condition was repeated three times. Functional images were acquired using the following parameters: repetition time of 2.35 s, voxel size of $3 \times 3 \times 3.5$ mm, with 80 voxels in the x-direction, 80 in the y-direction, and 40 in the z-direction. A total of 50 time points were acquired per run, resulting in a total scan duration of 117.5 s. The acquired NIfTI images were analyzed using Python with the Nilearn library. A voxel tSNR map was calculated by dividing the temporal mean by the temporal standard deviation (tSD) at each voxel. The main metrics computed were the full 3D tSNR and tSD map, the mean tSNR value across the phantom, and the corresponding mean tSD, which reflects absolute signal fluctuation. To assess whether device position affected signal quality, the tSNR and tSD values from each condition were compared.

Fig. 6: Position of the vacuum-switch in the MRI room. Shown here is the position at the bore entrance. The picture does not show the table inside the MRI bore, which is the case for the test.

III. Results

A. Temporal precision

Fig. 7 displays mean onset time (bars) and the associated 95 % confidence intervals (error bars) for every combination of delivery line length, flow rate, and configuration. Across both configurations, onset time lengthened as either tube length increased or flow rate decreased. At the lowest flow rate ($1\,\mathrm{L\,min^{-1}}$), latency for the Lorig configuration rose from roughly 2.3 s (1 m) to 8.3 s (9 m), whereas for the vacuum-switch latency spanned approximately 2.5 – 5.1 s over the same

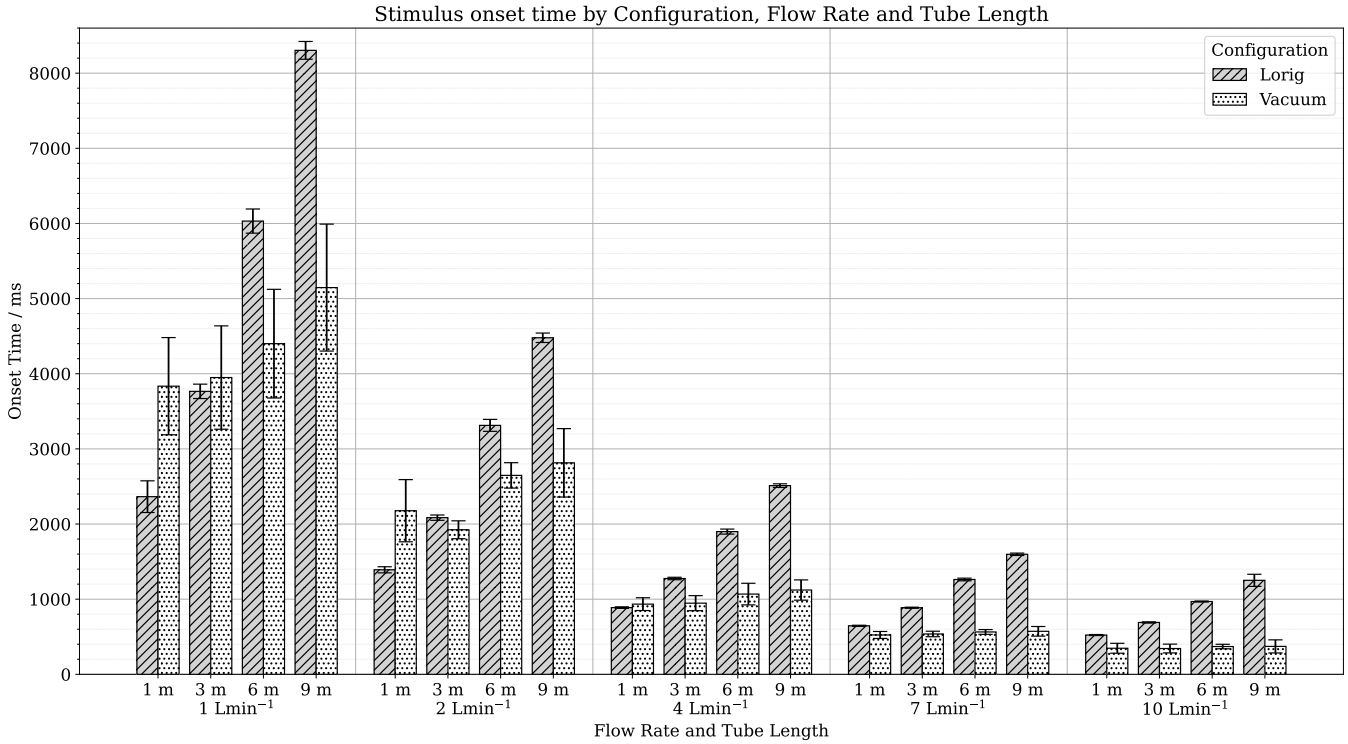

Fig. 7: Stimulus onset times for all combinations of flow rate, tube length, and configuration. Error bars represent 95 % confidence interval ($n = 10$).

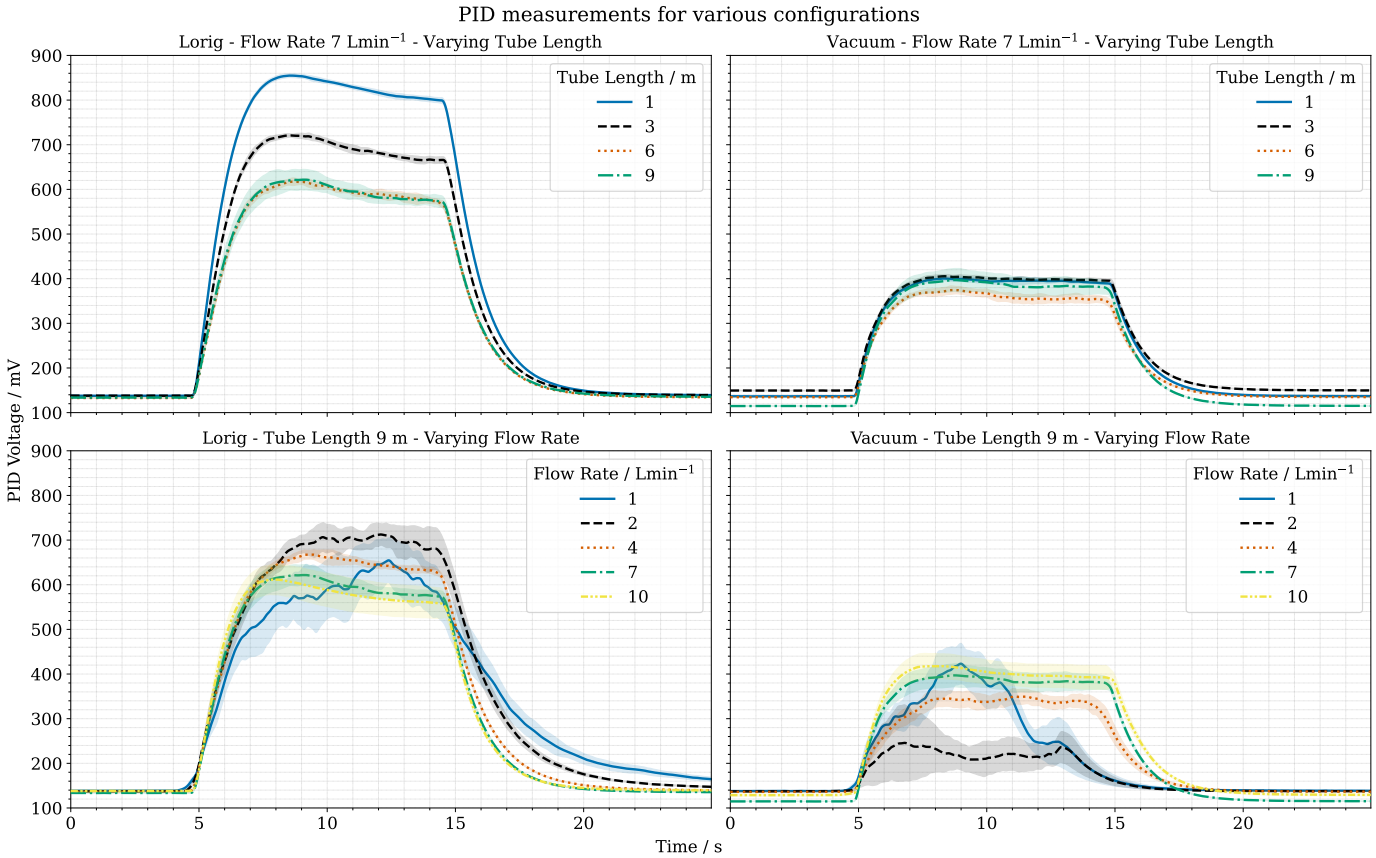

Fig. 8: Mean PID voltage traces for combinations of flow rate, tube length, and configuration. For clarity, the temporal latency has been offset so that each stimulus begins at $t = 5.0\,\mathrm{s}$. Top: stimulus shape at fixed flow rate (7 L/min) with varying tube lengths. Bottom: stimulus shape at fixed tube length (9 m) with varying flow rates. Left: Lorig configuration. Right: Vacuum configuration. Shaded areas represent 95 % confidence interval ($n = 10$).

lengths. Raising the flow to $2\,\mathrm{L\,min^{-1}}$ roughly halved these values, and at $4-10\,\mathrm{L\,min^{-1}}$, all conditions except the 9 m Lorig tube stayed below 2.0 s. For flow rates higher than $7\,\mathrm{L\,min^{-1}}$, the onset time for Lorig approximately doubles when comparing 1 m to 9 m tube length. For the vacuum configuration, however, there is no major increase in onset time. Latency precision also differed: vacuum error bars showed visibly wider confidence intervals than Lorig error bars, particularly at $1-2\,\mathrm{L\,min^{-1}}$. For both configurations, the confidence intervals narrow at high flow rates, but the vacuum confidence intervals remain visibly wider compared to Lorig.

B. Stimulus shape

Fig. 8 shows mean PID traces along with the 95 % confidence band for both configurations with varying tube lengths and flow rates. All traces show a visibly similar onset and offset shape. In the Lorig configuration, a pronounced concentration peak appeared in the first 2 to 3 seconds after onset, especially at flow rates of $4-10\,\mathrm{L\,min^{-1}}$. After this initial surge, the signal decayed by about 50 mV for the remaining stimulus window. The vacuum-switch configuration yielded a more flat stimulus profile for flow rates higher than $4\,\mathrm{L\,min^{-1}}$.

Higher flow rates generally resulted in more consistent stimulus shapes across both configurations, as reflected by narrower confidence intervals. At lower flow rates ($1-2\,\mathrm{L\,min^{-1}}$), onset and offset degradation were more pronounced in the Lorig configuration, exhibiting slower transitions and longer tails. However, trial-to-trial variability was higher in the vacuum configuration, which showed wider confidence bands at these lower flow rates.

Delivery tube length also played a major role in stimulus shape. For both configurations, longer tubes resulted in wider confidence bands, indicating increased variability. Additionally, for the Lorig configuration, increasing tube length led to a reduction in the maximum stimulus concentration. This effect is not observed in the vacuum configuration, which consistently delivered a maximum concentration approximately half that of the Lorig setup, regardless of tube length or flow rate.

C. Stimulus intensity

Fig. 9 plots the mean measured PID voltage recorded during 26 seconds of steady-state delivery as a function of dilution ratio. For both configurations, the concentration rose monotonically, but non-linearly: a ten-fold increase in dilution ratio from 2.5 % to 25 % boosted the Lorig signal from roughly 200 mV to 418 mV, whereas a comparable increment at the top end of the scale (70 % to 90 %) raised it by only 36 mV. The vacuum traces followed a similar curvature, but at lower absolute amplitudes, climbing from approximately 132 mV to 440 mV over the full range. Across the five repetitions acquired for each setting, 95 % confidence intervals never exceeded ±20 mV.

D. Cross contamination

Fig. 10 shows the PID voltage during a three stimulus sequence in which only the first stimulus contained isoamyl acetate. In the Lorig configuration, the second stimulus elicited a clear secondary peak of 22.3 mV above baseline, which is approximately 3.98 % of the primary response, which reached 561 mV above baseline. The third stimulus produced a smaller, yet still detectable, rise of 2.83 mV or 0.50 % of the primary response. In the vacuum-switch the mean primary peak reached 331 mV, while the second and third stimuli yielded peaks of 5.16 mV and 1.52 mV above baseline, corresponding to 1.56 % and 0.46 % of the primary response, respectively.

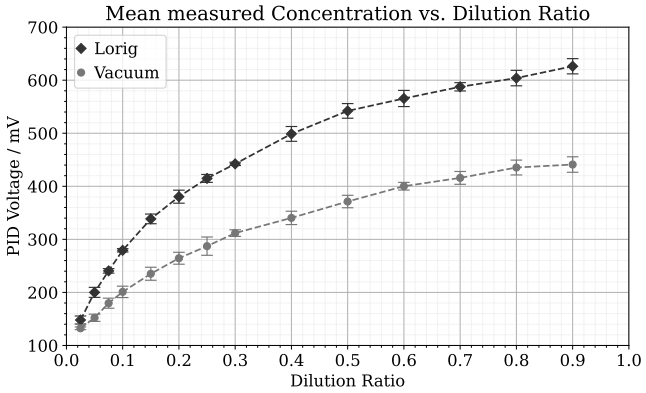

Fig. 9: Flow rate is $7\,\mathrm{L\,min^{-1}}$ and tube length is 9 m (MRI length). Mean of measured concentration for a 26-second window of constant stimulus. Error bars show 95 % confidence interval ($n = 5$).

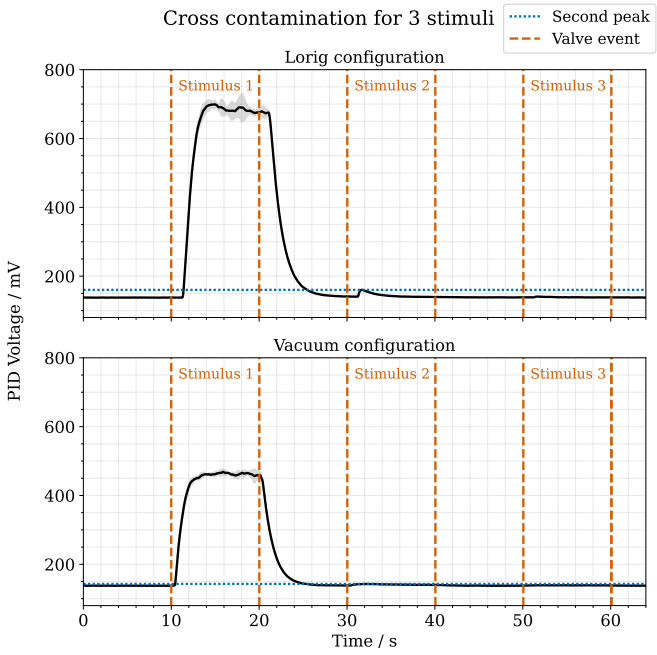

Fig. 10: PID mean traces showing cross-contamination across three sequential stimuli for both configurations (Top: Lorig, Bottom: Vacuum). The orange dashed line shows the valve switch timestamp. The blue dotted line shows the height of the secondary peak compared to the baseline. Shaded areas represent 95% confidence interval ($n = 5$).

E. Non-olfactory stimulation

Outlet flow measurements from the delivery line are shown in Fig. 11. With the Lorig system, each valve transition for a stimulus produced a drop to $6.0 \pm 0.5\,\mathrm{L\,min^{-1}}$ or −14.2 % relative to the $7\,\mathrm{L\,min^{-1}}$ target, which returned to a steady

plateau of approximately 6.6 L min^{-1} after 2 seconds. When switching back to control, a brief overshoot can be seen with a similar recovery time. In the vacuum-switch system, valve events generated deeper dips that reached as low as 2.0 L min^{-1} or −71.4 % from target flow rate, and recovery to baseline required approximately 1 s. However, during the 10-second stimulus blocks the mean flow tracked the target within approximately 0.2 L min^{-1}.

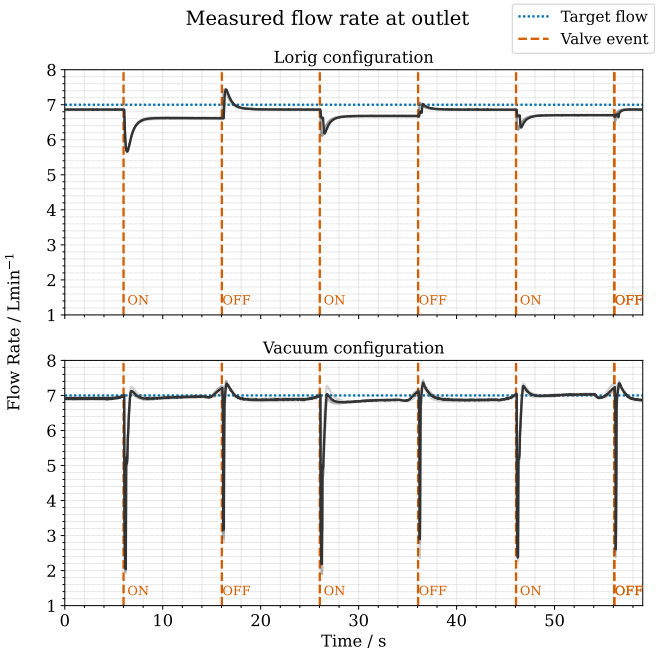

Fig. 11: Mean measured outlet flow rate during repeated odor ON/OFF transitions for both configurations(Top: Lorig, Bottom: Vacuum). Individual measurements are plotted with reduced opacity ($n = 3$).

F. MRI Compatibility

Table I lists the mean temporal signal-to-noise ratio (tSNR) and the corresponding mean temporal standard deviation (tSD) obtained of each position of the vacuum-switch. Across the three tested locations, outside the room (reference), at the bore entry, and directly beside the head coil, the phantom's average tSNR clustered between 37 – 38, varying by less than 2 % from the lowest to the highest measurement. The accompanying mean tSD values all lay within 0.797 – 0.802, a spread of only 0.005 units, and the repetition standard deviations for both metrics were similarly small with $\leq$0.73 for tSNR and $\leq$0.014 for tSD.

Figure 12 shows representative voxel maps of tSNR (top row) and tSD (bottom row) for the first run of each condition. In all three cases, the tSNR maps exhibited the same slight non-uniformity, with a small drop in tSNR in the center bottom of the phantom. The tSD maps displayed elevated noise along the outer rim of the phantom and lower values in the inner region, again across all three conditions. No additional artifacts or structured signal loss were visible in either metric when the device was positioned inside the bore or at the bore entry.

Table I: Mean and standard deviation (std) of tSNR and the corresponding tSD across three repetitions for each hardware position.

Condition	**tSNR** ($mean \pm std$)	**tSD** ($mean \pm std$)
Device next to coil	37.25 ± 0.57	0.802 ± 0.014
Device at bore entry	37.61 ± 0.21	0.797 ± 0.005
No device (reference)	37.05 ± 0.73	0.798 ± 0.010

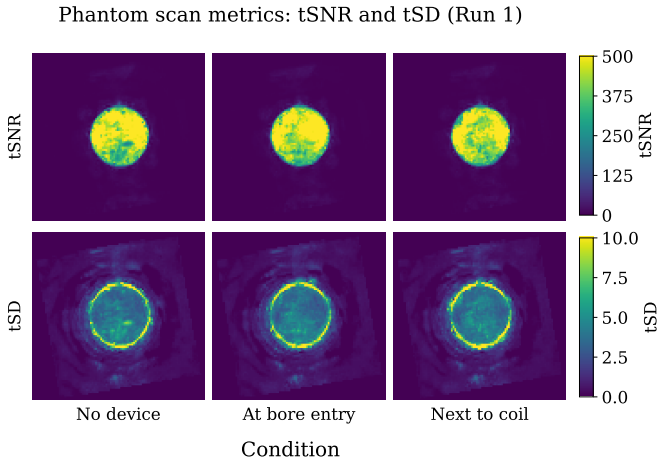

Fig. 12: Shows the tSNR and tSD voxel maps of the first run of each condition. The 3D voxel map is cut at the center of the phantom, which corresponds to $z = 0$. The tSNR and tSD for each voxel is averaged over the full temporal dimension.

IV. Discussion

This study investigated the performance of two types of MRI-compatible flow olfactometer architectures by performing a head-to-head comparison under identical conditions. The results demonstrate that design choices lead to quantifiable trade-offs in temporal precision, stimulus shape, concentration control, cross-contamination, and tactile stimulation. In the following sections, these findings are discussed in detail, along with their practical implications.

A. Vacuum-switching greatly reduces stimulus latency under MRI constraints at the cost of trial-to-trial variability

The latency measurements in Fig. 7 highlight the performance differences between the two configurations, especially when the olfactometer is positioned 6 – 9 m from the subject, as is typical in MRI settings. At 9 m tube length and 10 L min^{-1} flow, the vacuum-switch configuration achieved a latency of approximately 400 ms, comparable to the 480 ms rise time theorized by Sobel [19] for an 8 m tube at 15 L min^{-1}. Their setup used a wider 12 mm PTFE tube (versus 6 mm here) and placed the switching device closer to the subject (20 cm compared to 100 cm in this study). Across all tested flow rates, the vacuum-switch reduced mean onset latency by approximately 35 – 60 % compared to the Lorig configuration. However, this reduction came at the cost of increased trial-to-trial variability, as reflected by the broader confidence intervals of the vacuum-switch at all flow rates. The narrower confidence bands of the Lorig configuration suggest that this variability stems from the vacuum-switch itself. A possible cause is slight differences in the pressure required to overcome the internal static friction of the spring and sealing ring in the check valves of the vacuum-

switch. This might also explain why the confidence band narrows at higher flow rates for the vacuum configuration.

Another factor to consider is the role of preloading. In the present study, a fixed 2 s preload was used to fill the odorized line prior to stimulus onset. However, for lower flow rates in the vacuum configuration, the observed latency exceeded the preload time by 3 – 4 s. This implies that a preload duration of at least 5 s might be necessary to ensure the odor line is fully saturated before the switch. Extending the preload in this way increases the minimum inter-stimulus interval, which may constrain experiments.

In summary, the two configurations appear to be suited for distinct experimental priorities. The vacuum-switch design outperforms in applications that demand minimal onset time, such as synchronization with the respiratory cycle; however, its higher temporal variability may limit its use when exact stimulus onset timing is required. Conversely, the Lorig configuration, despite delivering a slower average onset, offers greater consistency across trials. Regardless of configuration, increasing the flow rate remains a reliable strategy to reduce both mean latency and variability.

B. Stimulus shape is primarily governed by flow rate

The PID measurements suggest that flow rate, rather than configuration alone, is the principal factor influencing stimulus shape. While both system architecture and delivery tube length play a role, the degradation observed at lower flow rates ($1 – 2\,\mathrm{L\,min^{-1}}$) was more pronounced across both configurations. In the Lorig configuration, extended offset tails were observed, likely due to increased diffusion of odorant within the delivery line. In contrast, the vacuum-switch configuration produced cleaner offsets, even at low flow rates, suggesting that the vacuum-switch is less affected by diffusion. Trial-to-trial variability followed a similar trend. At lower flow rates, both systems showed increased confidence intervals, but this effect was particularly evident in the vacuum configuration.

One noticeable characteristic of the Lorig shape is the concentration peak at stimulus onset, particularly at higher flow rates. This initial surge is likely due to odorant accumulation in the canister headspace while the solenoid valve remains closed. When the valve is activated, the more concentrated odorized air is delivered before achieving equilibrium with the air stream. The vacuum configuration does not show this, which can likely be attributed to the 2-second preload phase, which flushes the concentrated headspace prior to stimulus delivery, thereby reaching equilibrium before the stimulus onset.

In practice, both configurations can produce a sufficiently square stimulus shape, with flow rate emerging as the primary determinant of quality. The vacuum-switch configuration offers cleaner stimulus termination at low flow rates but at the cost of increased variability across trials. These findings suggest that selecting an appropriate flow rate is key to balancing stimulus quality, subject comfort, and timing precision. The vacuum-switch may be preferred for applications requiring sharp stimulus cutoff and flat concentration plateau, while the Lorig configuration provides greater consistency where variability is a concern.

C. Perceived odor intensity is shaped by mechanical, chemical, and psychophysical factors

Our measurements show that the mechanical characteristics of the olfactometer play an important role in the vapor concentration delivered to the participant. In the Lorig configuration, increasing the length of the delivery line led to a clear reduction in peak concentration, see Fig. 8. This result aligns with the findings of Johnson and Sobel [11], who demonstrated that greater flow resistance due to longer tubing raises upstream pressure in the odorant canister, which in turn suppresses evaporation and reduces the vapor concentration reaching the outlet. This mechanism likely explains why the Lorig configuration consistently delivered higher concentrations than the vacuum-switch design at all dilution ratios. The additional flow resistance introduced by the vacuum-switch's check valves further increases upstream pressure, limiting evaporation and reducing the final concentration. In addition, we observed a non-linear relationship between dilution ratio and measured vapor concentration in Fig. 9. This can be attributed to the combined effect of pressure differentials and increased flow rates through the odorant canister at higher dilution ratios. Elevated flow rates result in a higher pressure due to increased resistance and reduce the residence time of the carrier air over the liquid surface, both of which contribute to reduced vapor output.

Although this study focused on mechanical factors, it is important to consider that the chemical properties of the odorant-solvent mixture also play a critical role in evaporation behavior. According to Raoult's law for ideal mixtures, the vapor pressure, which is proportional to evaporation rate [29], of an odorant in solution should be proportional to its mole fraction, and by extension, the evaporation rate is expected to decrease linearly with increasing dilution. However, as Jennings et al. [30] demonstrated, the actual relationship between liquid and vapor phase concentrations often deviates from this ideal. Their study across a broad set of odorant-solvent pairs showed frequent positive deviations, where vapor concentrations exceeded predictions based on Raoult's law. This behavior is driven by specific odorant-solvent interactions that alter volatility, making it challenging to predict without experimental testing.

In addition, temperature plays a central role in determining vapor pressure and thus evaporation rate. The Antoine equation or its refinements, such as the full-range vapor pressure equation proposed by Lee [31], describe how vapor pressure rises exponentially with temperature. Even minor changes in temperature can shift the vapor concentration delivered to the participant, which shows the importance of controlling or at least monitoring temperature during experiments.

Finally, it is crucial to distinguish between vapor concentration and perceived intensity. While vapor concentration can be measured physically, perceived intensity follows a psychophysical relationship that is not uniform across odorants. As shown by Doty [32], the perceived intensity of an odorant generally follows a power function of concentration, with the exponent varying between substances. This means that two odorants at the same vapor concentration can result in very

different perceived intensities.

Taken together, these findings highlight that the final odor perception depends on a combination of mechanical, chemical, and psychophysical factors. From a practical standpoint, the lower output concentration of the vacuum-switch configuration or the concentration losses associated with long tubing in the Lorig setup can be compensated by adjusting the liquid dilution in the canisters. However, such adjustments require more than simply scaling the liquid concentration linearly, careful calibration and understanding of the specific odorant-solvent interactions are necessary to achieve the desired vapor levels. Notably, both systems demonstrated high repeatability across trials, as indicated by narrow confidence intervals at all dilution ratios. This suggests that once calibrated, either configuration is capable of delivering consistent and reliable concentrations in a controlled environment.

D. Vacuum-switching minimizes cross-contamination but magnifies tactile cues

The results from the cross-contamination and non-olfactory experiments highlight a clear trade-off between stimulus isolation and tactile stability for the two configurations. From a contamination perspective, the vacuum-switch design demonstrated superior performance in limiting cross-contamination. The secondary concentration peaks observed with the vacuum-switch were minimal compared to those seen with the Lorig configuration. This indicates that residual vapor persists within the Lorig mixing manifold, likely due to the shared pathway used for both odorized and clean air and the presence of dead air spaces where odorant can linger. In contrast, the vacuum-switch routes clean air through a separate path that bypasses the mixing manifold entirely, effectively preventing residual odor from reaching the subject between stimuli.

An additional factor to consider is the difference in control sequences used for the two configurations. The vacuum-switch setup employed a more advanced sequence, including a 5% boost in total flow during stimulus delivery to help compensate for small leaks and bring the measured flow closer to the target value. This adjustment was not applied in the Lorig configuration, giving the vacuum setup a slight advantage in maintaining the target flow rate during testing. From a tactile perspective, the vacuum-switch configuration still performs worse due to noticeable flow fluctuations during stimulus transitions. Each toggle of the 3-way valve causes a visible drop in flow rate, resulting from the rerouting of airflow and the time required for the check valves to switch over. Although careful calibration of the MFC flow rates and adjustment of the vacuum pressure have helped to reduce this effect, the fluctuations remain pronounced. In contrast, the Lorig configuration produces smaller flow deviations and transitions more gradually, though with a slower return to baseline. The practical impact of these fluctuations depends on the delivery interface. In the present MRI setup, where odorant was delivered through an oxygen mask or free tube positioned parallel to the subject's face, the flow dips were not noticeable during pilot testing. However, in a more enclosed system, such as one using nasal cannulae, these fluctuations could be perceived as brief puffs or drops, introducing unintended tactile cues.

These findings suggest a configuration-dependent recommendation. In studies utilizing nasal cannulae, where the airflow is delivered directly into the nostrils, and any tactile fluctuations are likely to be perceptible, the Lorig-style configuration is better suited due to its greater flow stability. Conversely, when using low-volatility odorants, which are more prone to lingering in the system and may compromise stimulus purity, the vacuum-switch configuration is recommended for its lower susceptibility to cross-contamination. A potential improvement to the Lorig design could involve adding a control line and drain system after the mixing manifold to flush the manifold between stimuli, details of this proposal are provided in Appendix E.

E. Limitations

Several limitations of the present study should be acknowledged. First, the measurement of stimulus onset and offset dynamics was constrained by the temporal response characteristics of the PID. The onset and offset shapes of all measured stimuli were nearly identical across conditions, regardless of flow rate or tube length, indicating that the observed rise and decay shapes reflect intrinsic sensor dynamics rather than the true stimulus shape. According to the manufacturer, the time required for the sensor signal to reach 50% (T50) and 90% (T90) of its maximum value is 0.76 s and 2.53 s, respectively, consistent with these shape observations. To improve responsiveness, the filter element of the PID was removed following consultation with the manufacturer. All data in this study was collected using this modified configuration, which yielded slightly improved onset and offset responses. For future research, a PID with higher temporal resolution should be selected.

The experimental scope was also limited to a comparison between two specific configurations: the Lorig-style design and the vacuum-switch architecture. While these represent two widely used approaches in flow olfactometry, many other system designs and hybrid configurations exist. Furthermore, this study focused only on the switching mechanism, flow rate, tube length, and air dilution ratio, although precise odor delivery depends on additional factors such as the evaporation method, delivery interface, and synchronization with respiration. Future research should explore alternative design variations and further investigate these additional factors to support the development of more optimized olfactometry systems.

V. Conclusion

This study evaluated two MRI-compatible flow olfactometer architectures: a vacuum-switch design and a Lorig-style design, both built around the same modular hardware base. Experimental tests covered temporal precision, stimulus shape, achievable intensity, cross-contamination, tactile flow cues, and MRI compatibility. The vacuum-switch configuration produced the fastest odor onsets at the cost of more variation in onset timing. It also featured a more desirable square

pulse shape at high flow rates and showed the lowest cross-contamination between sequential stimuli. These advantages came at the cost of deeper airflow fluctuations during valve transitions and a lower achievable concentration range. The Lorig-style configuration delivered higher peak concentrations and steadier flow at the delivery line outlet. Its timing and pulse shape, however, degraded in proportion to tube length and flow rate, and more residual odor was present in subsequent stimuli. Together, the results highlight clear trade-offs rather than a single best solution. Experiments that depend on low latency will benefit from the vacuum-switch layout, while studies that prioritize timing precision over latency or require minimal tactile stimulation may prefer the simpler Lorig approach. These findings provide a quantitative basis for making better-informed choices in olfactometer design and parameter selection for MRI olfactory studies, ultimately supporting research aimed at advancing our understanding of the neural mechanisms of olfaction in neurodegenerative diseases.

REFERENCES

[1] R. L. Doty, *Handbook of Olfaction and Gustation*. John Wiley & Sons, Jul. 2015.

[2] A. W. Bacon, M. W. Bondi, D. P. Salmon, and C. Murphy, "Very Early Changes in Olfactory Functioning Due to Alzheimer's Disease and the Role of Apolipoprotein E in Olfaction," *Annals of the New York Academy of Sciences*, vol. 855, no. 1, pp. 723–731, 1998.

[3] J. Wang, P. J. Eslinger, R. L. Doty, E. K. Zimmerman, R. Grunfeld, X. Sun, M. D. Meadowcroft, J. R. Connor, J. L. Price, M. B. Smith, and Q. X. Yang, "Olfactory deficit detected by fMRI in early Alzheimer's disease," *Brain Research*, vol. 1357, pp. 184–194, Oct. 2010.

[4] E. Wehling, H. Naess, D. Wollschlaeger, H. Hofstad, A. Bramerson, M. Bende, and S. Nordin, "Olfactory dysfunction in chronic stroke patients," *BMC Neurology*, vol. 15, no. 1, p. 199, Oct. 2015.

[5] M. Schön, D. M. Cruz, R. Tomás, F. Sotero, P. N. Alves, and P. Canhão, "Assessing Taste and Smell Dysfunction in Acute and Chronic Stroke Patients: Insights From an Adapted Bedside Questionnaire," *European Journal of Neurology*, vol. 32, no. 5, p. e70089, 2025.

[6] D. G. Laing, "Identification of single dissimilar odors is achieved by humans with a single sniff," *Physiology & Behavior*, vol. 37, no. 1, pp. 163–170, Jan. 1986.

[7] A. Dravnieks, "Instrumental aspects of olfactometry," *Methods in olfactory research*, pp. 1–61, 1975.

[8] C. J. Li, Q. Yao, Y. L. Liu, Y. M. Wang, and S. H. Feng, "Application Research on Objective Evaluation of Vehicle Interior Odor Based On Weber-Fechner Law," *IOP Conference Series: Earth and Environmental Science*, vol. 657, no. 1, p. 012019, Feb. 2021.

[9] M. Vigouroux, B. Bertrand, V. Farget, J. Plailly, and J. Royet, "A stimulation method using odors suitable for PET and fMRI studies with recording of physiological and behavioral signals," *Journal of Neuroscience Methods*, vol. 142, no. 1, pp. 35–44, Mar. 2005.

[10] A.-K. Bestgen, P. Schulze, L. Kuchinke, B. Suchan, T. Derdak, T. Otto, B. Jettkant, and K. Sucker, "An extension of olfactometry methods: An expandable, fully automated, mobile, MRI-compatible olfactometer," *Journal of Neuroscience Methods*, vol. 261, pp. 85–96, Mar. 2016.

[11] B. N. Johnson and N. Sobel, "Methods for building an olfactometer with known concentration outcomes," *Journal of Neuroscience Methods*, vol. 160, no. 2, pp. 231–245, Mar. 2007.

[12] T. S. Lorig, D. G. elmes, D. H. Zald, and J. V. Pardo, "A computer-controlled olfactometer for fMRI and electrophysiological studies of olfaction," *Behavior Research Methods, Instruments, & Computers*, vol. 31, no. 2, pp. 370–375, Jun. 1999.

[13] F. Vedaei, M. Fakhri, M. H. Harirchian, K. Firouznia, Y. Lotfi, and M. Ali Oghabian, "Methodological considerations in conducting an olfactory fMRI study," *Behavioural Neurology*, vol. 27, no. 3, pp. 267–276, Jan. 2013.

[14] S. B. Lowen and S. E. Lukas, "A low-cost, MR-compatible olfactometer," *Behavior Research Methods*, vol. 38, no. 2, pp. 307–313, May 2006.

[15] S. Borromeo, J. A. Hernandez-Tamames, G. Luna, F. Machado, N. Malpica, and A. Toledano, "Objetive assessment of olfactory function using functional magnetic resonance (fMRI)," in *2009 IEEE International Workshop on Medical Measurements and Applications*, May 2009, pp. 79–82.

[16] A. Stankewitz, H. Voit, U. Bingel, C. Peschke, and A. May, "A new trigemino-nociceptive stimulation model for event-related fMRI," *Cephalalgia*, vol. 30, no. 4, pp. 475–485, 2010.

[17] I. Cuevas, B. Gérard, P. Plaza, E. Lerens, O. Collignon, C. Grandin, A. G. De Volder, and L. Renier, "Development of a fully automated system for delivering odors in an MRI environment," *Behavior Research Methods*, vol. 42, no. 4, pp. 1072–1078, Nov. 2010.

[18] G. Kobal, "Pain-related electrical potentials of the human nasal mucosa elicited by chemical stimulation," *Pain*, vol. 22, no. 2, pp. 151–163, Jun. 1985.

[19] N. Sobel, V. Prabhakaran, J. Desmond, G. Glover, E. Sullivan, and J. Gabrieli, "A method for functional magnetic resonance imaging of olfaction," *Journal of Neuroscience Methods*, vol. 78, no. 1-2, pp. 115–123, Dec. 1997.

[20] V. A. Benignus and J. D. Prah, "A computer-controlled vapor-dilution olfactometer," *Behavior Research Methods & Instrumentation*, vol. 12, no. 5, pp. 535–540, Sep. 1980.

[21] J. N. Lundström, A. R. Gordon, E. C. Alden, S. Boesveldt, and J. Albrecht, "Methods for building an inexpensive computer-controlled olfactometer for temporally-precise experiments," *International Journal of Psychophysiology*, vol. 78, no. 2, pp. 179–189, Nov. 2010.

[22] L. F. Valdez and J. M. Gutiérrez, "Portable olfactometric platform," in *2016 Global Medical Engineering Physics Exchanges/Pan American Health Care Exchanges (GMEPE/PAHCE)*, Apr. 2016, pp. 1–6.

[23] P. Andrieu, V. Bonnans, J. Meneses, J.-L. Millot, T. Moulin, and T. Gharbi, "A modular, computer-controlled system for olfactory stimulation in the MRI environment," *Behavior Research Methods*, vol. 46, no. 1, pp. 178–184, Mar. 2014.

[24] C. Sezille, B. Messaoudi, A. Bertrand, P. Joussain, M. Thévenet, and M. Bensafi, "A portable experimental apparatus for human olfactory fMRI experiments," *Journal of Neuroscience Methods*, vol. 218, no. 1, pp. 29–38, Aug. 2013.

[25] C. M. Philpott, P. C. Goodenough, C. R. Wolstenholme, and G. E. Murty, "Which solvent for olfactory testing?" *Clinical Otolaryngology and Allied Sciences*, vol. 29, no. 6, pp. 667–671, Dec. 2004.

[26] L. Gorodisky, E. Livne, T. Weiss, A. Weissbrod, R. Weissgross, E. Mishor, E. Furman-Haran, and N. Sobel, "Odor Canopy: A Method for Comfortable Odorant Delivery in MRI," *Chemical Senses*, vol. 46, p. bjaa085, Jan. 2021.

[27] R. A. De Wijk, W. Vaessen, J. Heidema, and E. P. Köster, "An injection olfactometer for humans and a new method for the measurement of the shape of the olfactory pulse," *Behavior Research Methods, Instruments, & Computers*, vol. 28, no. 3, pp. 383–391, Sep. 1996.

[28] A. Bahremand, M. Manetta, J. Lai, B. Lahey, C. Spackman, B. Smith, R. Gerkin, and R. Likamwa, "The Smell Engine: A system for artificial odor synthesis in virtual environments," in *Proceedings - 2022 IEEE Conference on Virtual Reality and 3D User Interfaces, VR 2022*, 2022, pp. 241–249.

[29] D. Mackay and I. van Wesenbeeck, "Correlation of Chemical Evaporation Rate with Vapor Pressure," *Environmental Science & Technology*, vol. 48, no. 17, pp. 10 259–10 263, Sep. 2014.

[30] L. Jennings, E. Williams, S. Caton, M. Avlas, and A. Dewan, "Estimating the relationship between liquid- and vapor-phase odorant concentrations using a photoionization detector (PID)-based approach," *Chemical Senses*, vol. 48, p. bjac038, Dec. 2022.

[31] J.-Y. Lee, "Derivation of full range vapor pressure equation from an arbitrary point," *Chemical Engineering Communications*, vol. 212, no. 2, pp. 250–259, Feb. 2025.

[32] R. L. Doty, "An examination of relationships between the pleasantness, intensity, and concentration of 10 odorous stimuli," *Perception & Psychophysics*, vol. 17, no. 5, pp. 492–496, Sep. 1975.

Appendix A
Bill of Materials

Category	Part #	Part Name	Description	Supplier	Qty	Unit Cost (CHF)	Total Cost (CHF)
Electronics	1	Raspberry Pi	Raspberry pi 4 model B	Conrad	1	53.95	53.95
	2	Arduino	Arduino Mega2560	Conrad	1	35.95	35.95
	3	PSU	Mean Well 24 V DC 13.4A 321.6W	Conrad	1	51.95	51.95
	4	16-Channel Relay	TRU COMPONENTS TC-9445344	Conrad	1	21.95	21.95
	5	DC/DC Converter	24 V DC 5 V DC 3A 15W	DigiKey	1	7.48	7.48
	6	Power Distribution Block	2903717	DigiKey	1	64.24	64.24
	7	USB A to RS485	FIT0874	DigiKey	3	4.90	14.70
	8	M8 end cable	RKMV 4-225/5 M	Distrelec	3	10.08	30.24
	9	Splicing Connector	222-413	Distrelec	12	0.60	7.20
	10	4-Channel Relay	Purecrea 4-channel relay module	Amazon	1	5.06	5.06
	11	Ethernet to USB A	USB C to Ethernet Adapter with USB 3.0 to RJ45	Amazon	1	7.77	7.77
Valves and Flow control	12	Mass Flow Controller 20LPM	Sensirion SFC6000D-20SLM	DigiKey	2	308.75	617.50
	13	Mass Flow Controller 50LPM	Sensirion SFC6000D-50SLM	DigiKey	1	308.75	308.75
	14	Vacuum Piston Pump	VP750-30L, 120l/min	VacuumChambers	1	407.01	407.01
	15	3/2 Solenoid Valve	MHP2-M1H-3/2G-M5	Festo	16	63.16	1010.56
	16	Valve Cable	KMYZ-4-24-2,5-B	Festo	16	7.31	116.96
	17	Manifold Block	MHP2-PR10-3	Festo	1	94.25	94.25
	18	Manifold Block	MHP2-PR8-3	Festo	1	80.46	80.46
	19	Cover Plate	MHAP2-BP-3	Festo	2	4.76	9.52
	20	3/2 Solenoid Valve	MHE3-M1H-3/2G-1/8-K	Festo	1	62.74	62.74
	21	Filter regulator	MS4-LFR-1/4-D7-CRM-AS	Festo	1	67.99	67.99
	22	Activated carbon filter	MS4-LFX-1/4-R	Festo	1	66.05	66.05
	23	Ball valve	QH-1/4	Festo	2	20.00	40.00
Tubing and Fittings	24	Tee Union PTFE	UNION TEE 6 MMOD X 6 MMOD X 6 MMOD	TU-LOK	3	12.00	36.00
	25	Male Connector PTFE	MALE CONNECTOR 6 MMOD X 1/8" BSPM	TU-LOK	18	8.00	144.00
	26	Plugs PTFE	PLUG 1/8" BSPM	TU-LOK	18	8.00	144.00
	27	Check Valve PTFE	CHECK VALVE 6 MMOD X 6 MMOD	TU-LOK	21	32.00	672.00
	28	Manifold Block PTFE	MANIFOLD - 16 OUTLETS, 1 INLET & 1 DRAIN - ALL 1/8" BSPF	TU-LOK	1	350.00	350.00
	29	Tubing PTFE	PTFE-tube, 6x4mm, natural	Landefeld	25	10.44	261.00
	30	Gasket PTFE	Gasket PTFE for G1/8	Landefeld	30	0.30	9.00
	31	Distributor Block ALU	Distributor bar 2x G 1/4"-12xG 1/8", Anodized aluminium	Landefeld	1	30.55	30.55
	32	Flow restrictor 6mm	AS1002F-06-J - AS Series Tube Speed Controller	Distrelec	2	10.08	20.16
	33	PU Tubing 50m	PUN-H-6X1-NT	Festo	2	54.00	108.00
	34	Push-in fitting G1/8 SS	NPQR-DK-G18-Q6	Festo	10	14.80	148.00
	35	Push-in fitting G1/4 SS	NPQR-DK-G14-Q6	Festo	6	18.38	110.28
	36	Distributor block ALU	FR-4-1/4	Festo	1	14.38	14.38
	37	Blanking plug G1/4	B-1/4-F1A	Festo	10	1.45	14.50
	38	Blanking plug G1/8	B-1/8-F1A	Festo	10	1.20	12.00
	39	Push-in fitting L M5	QSML-M5-6	Festo	10	3.66	36.60
	40	Push-in fitting M5	QSM-M5-6-I	Festo	10	2.71	27.10
	41	Push-in fitting M7	QSM-M7-6-I	Festo	40	2.45	98.00
	42	Push-in T-connector	QSMT-6	Festo	10	4.49	44.90
	43	Push-in fitting G1/4	QS-G1/4-6	Festo	10	2.53	25.30
	44	Double nipple 2xG1/4	NPFC-D-2G14-M	Festo	10	8.60	86.00
Bottles and consumables	45	Gas washing bottle	100ml - Plastic PP	LaborXing	16	27.00	432.00
	46	Oxygen mask	Sauerstoffmaske EcoLite	LungenLiga	3	2.20	6.60
	47	Bottle O-ring	O-ring 25mmX31mmX3mm	Amazon	2	5.01	10.02
	48	Bottle Closing Ring	Dichtungsring - 39mm	Amazon	4	7.77	31.08
	49	Bottle Connection Washer	Rubber washer 6mmX12mmX4.5mm	Amazon	2	5.96	11.92
	50	Check Valve O-ring	O-ring 6mmX10mmX2mm	Amazon	1	6.65	6.65
Enclosure and Mounting	51	Enclosure Box ALU	Alutec Classic 48	Galaxus	2	95.95	191.90
	52	Computer Fan	80mm 24V	Amazon	2	6.49	12.98
	53	Dust Filter Fan	Dust filter computer fan 80mm	Amazon	1	7.62	7.62
	54	Rubber Strip	Edge Protection Sheet 1.6 mm x 6 m	Amazon	1	15.35	15.35
	55	Bolts and Nuts	Black 260pcs M3	Amazon	1	7.67	7.67
	56	Bolts and Nuts	440 Piece M3 Screws Nuts	Amazon	1	7.65	7.65
	57	Acrylic sheets	Acrylic Glass Sheet Transparent 3 mm, DIN A2 (420 x 594 mm)	Amazon	2	16.17	32.34
Sensors	58	PID Sensor	PIDX-A-04K0-4,000 ppm PID sensor	Alphasense	1	352.20	352.20
	59	Sensor Mounting Board	PID PCB mounting board	Alphasense	1	36.90	36.90
	60	Flow Sensor	Sensirion SFM4300-20-P	DigiKey	1	103.99	103.99
Total							**6840.92**

APPENDIX B
ROS DIAGRAMS

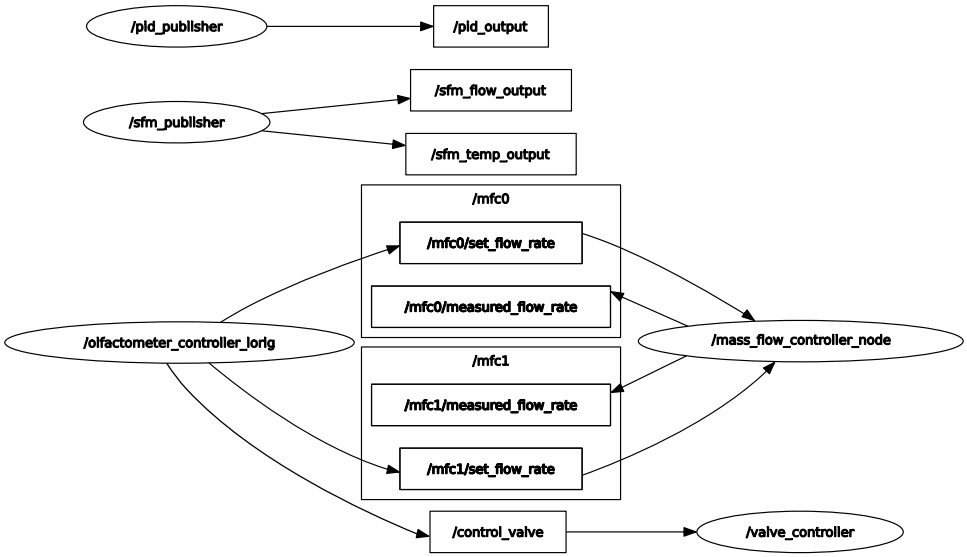

(a) Nodes and topics in Lorig configuration

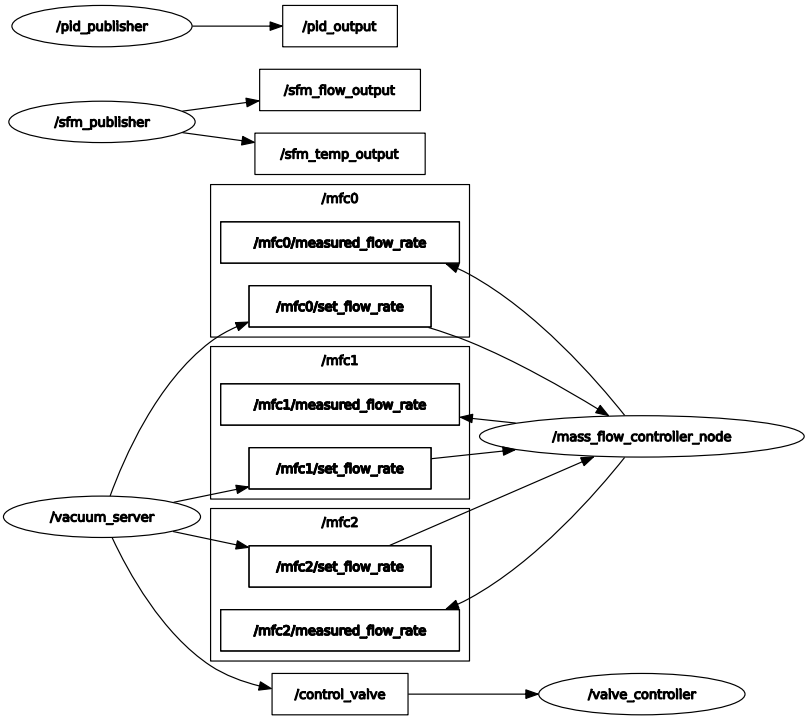

(b) Nodes and topics in Vacuum configuration

Diagrams showing ROS 2 nodes (ovals) and topics (rectangles) running on the Raspberry Pi for both configurations. The diagrams are made with the rqtgraph package. */pid_publisher* publishes PID data received from Teensy, */sfm_publisher* publishes flow rate and temperature data from the Sensiron flow rate sensor, */mass_flow_controller_node* sets flow rate's for each MFC and receives measured flow rate data back from each MFC, */valve_controller* communicates with the Arduino to control solenoid valves. The difference between the two configurations is the lack of MFC 2 for the Lorig configuration, and the main control node. For the vacuum configuration, this is the */vacuum_server* node, but for the Lorig configuration, the */olfactometer_controller_lorig* node is used. All code can be found in the GitHub repository: https://github.com/DART-Lab-LLUI/olfacto_ros2.git

Appendix C
Electrical Schematic

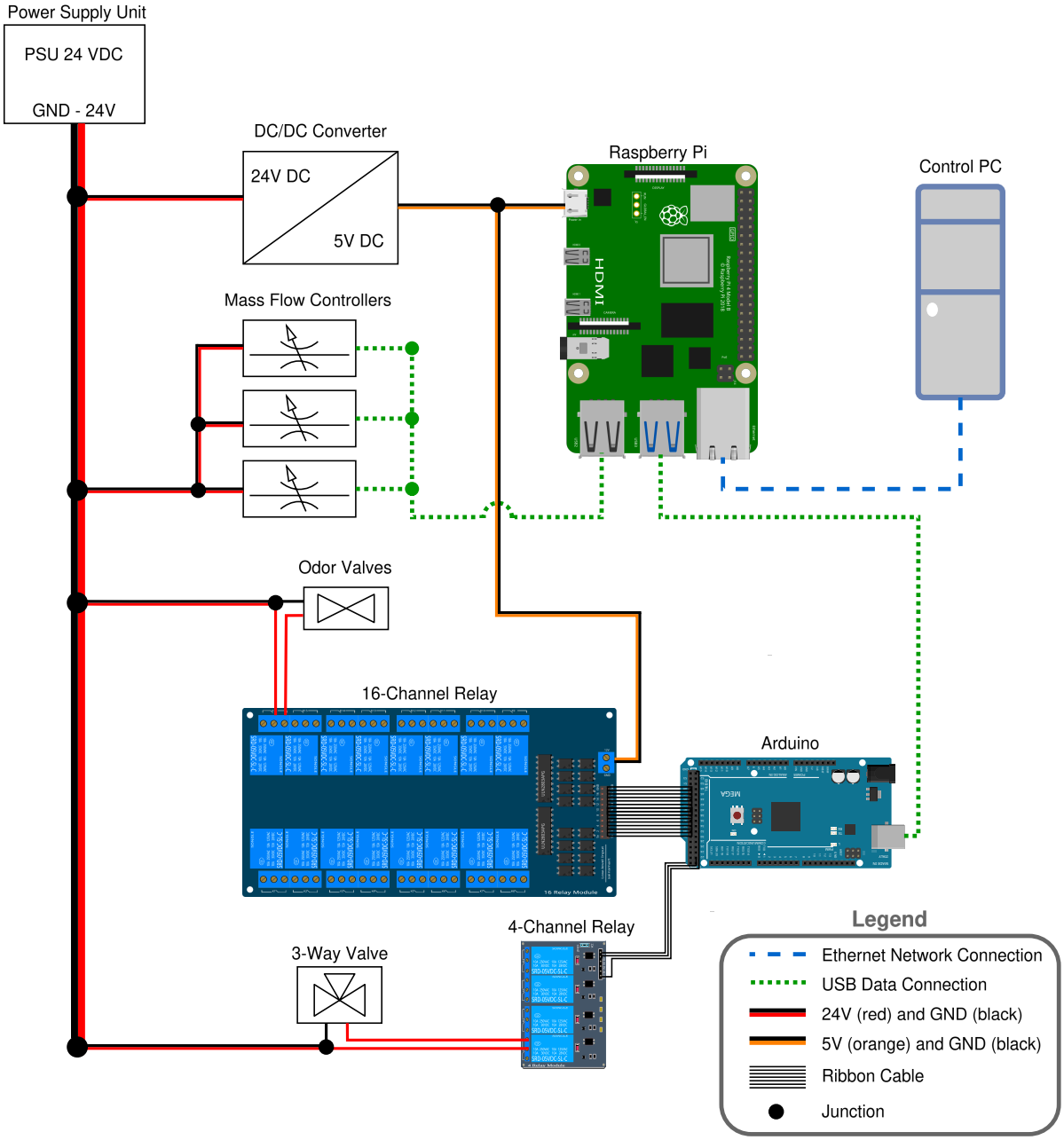

This diagram shows a basic overview of the power and data connections of the main electrical and pneumatic components in the system. The 24 VDC power supply provides power to the mass flow controllers, the odor valves, the 3-way valve, and the DC/DC converter. The mass flow controllers are daisy-chained together for both power and data, and communicate with the Raspberry Pi via USB connection. The DC/DC converter supplies 5 VDC to the Raspberry Pi and the 16-channel relay module. The Raspberry Pi also connects to the control PC via Ethernet and to the Arduino via USB. The Arduino controls both the 16-channel and 4-channel relay modules using a ribbon cable connection. The 3-way valve is powered directly from the 24 VDC supply and switched via the 4-channel relay, which is itself powered by the Arduino. For simplicity, only one of the 16 odor solenoid valves controlled by the 16-channel relay is shown. The diagram applies to both the Lorig and vacuum-switch configurations; however, in the Lorig configuration, the 3-way valve and third mass flow controller are not used.

Appendix D
MFC Flow Rates

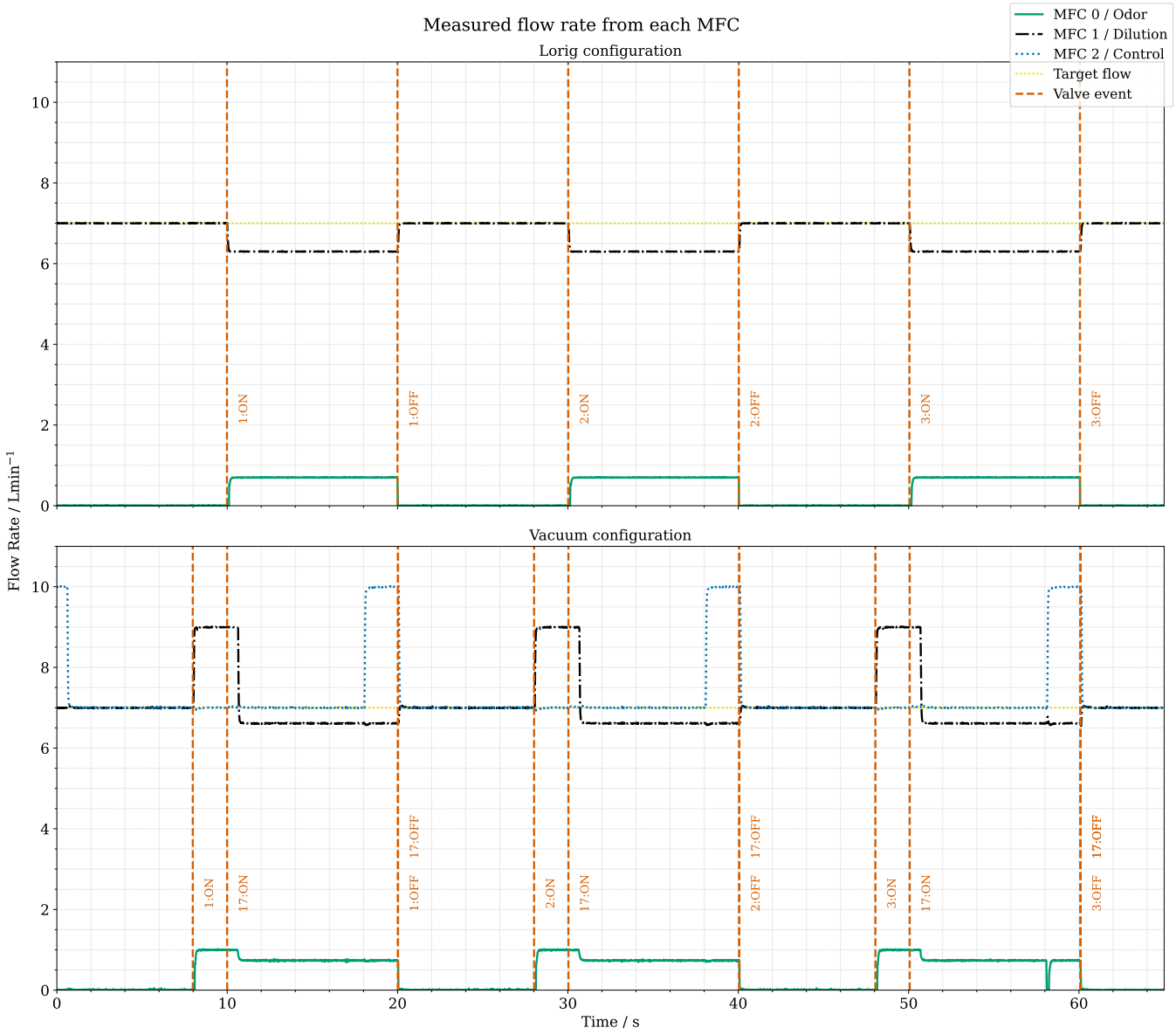

This plot shows the measured flow rates from each mass flow controller (MFC) during one of the tactile stimulation measurements, with a target flow rate of $7\,\mathrm{L\,min^{-1}}$ and a 10 % dilution ratio. The vertical dashed lines indicate valve events: the number refers to the actuated valve (1, 2, or 3 for the odor valves, and 17 for the 3-way vacuum valve), while ON or OFF indicates whether the valve is opened or closed, respectively. The difference in control sequence between the two configurations is clearly visible. In the Lorig configuration, the control sequence is straightforward: during stimulus periods, the MFCs are set to achieve the desired dilution ratio by providing $0.7\,\mathrm{L\,min^{-1}}$ from MFC 0 (odor line) and $6.3\,\mathrm{L\,min^{-1}}$ from MFC 1 (dilution line). In contrast, the vacuum configuration employs a more complex sequence to achieve smoother transitions during switching. During the 2-second preload phase, the total flow rate is temporarily increased to $10\,\mathrm{L\,min^{-1}}$ while maintaining the 10 % dilution ratio ($1\,\mathrm{L\,min^{-1}}$ from MFC 0 and $9\,\mathrm{L\,min^{-1}}$ from MFC 1). This elevated flow continues for 0.6 s after the 3-way valve is actuated. Following this, the flow rates are adjusted to maintain the dilution ratio, with the total flow boosted by 5 % ($0.735\,\mathrm{L\,min^{-1}}$ from MFC 0 and $6.615\,\mathrm{L\,min^{-1}}$ from MFC 1). When switching back to no stimulus, the control line is briefly boosted to $10\,\mathrm{L\,min^{-1}}$; however, because of the smaller total volume in the vacuum line, extending this boost after the valve switch was found to be unnecessary.

APPENDIX E
LORIG REVISION PROPOSAL

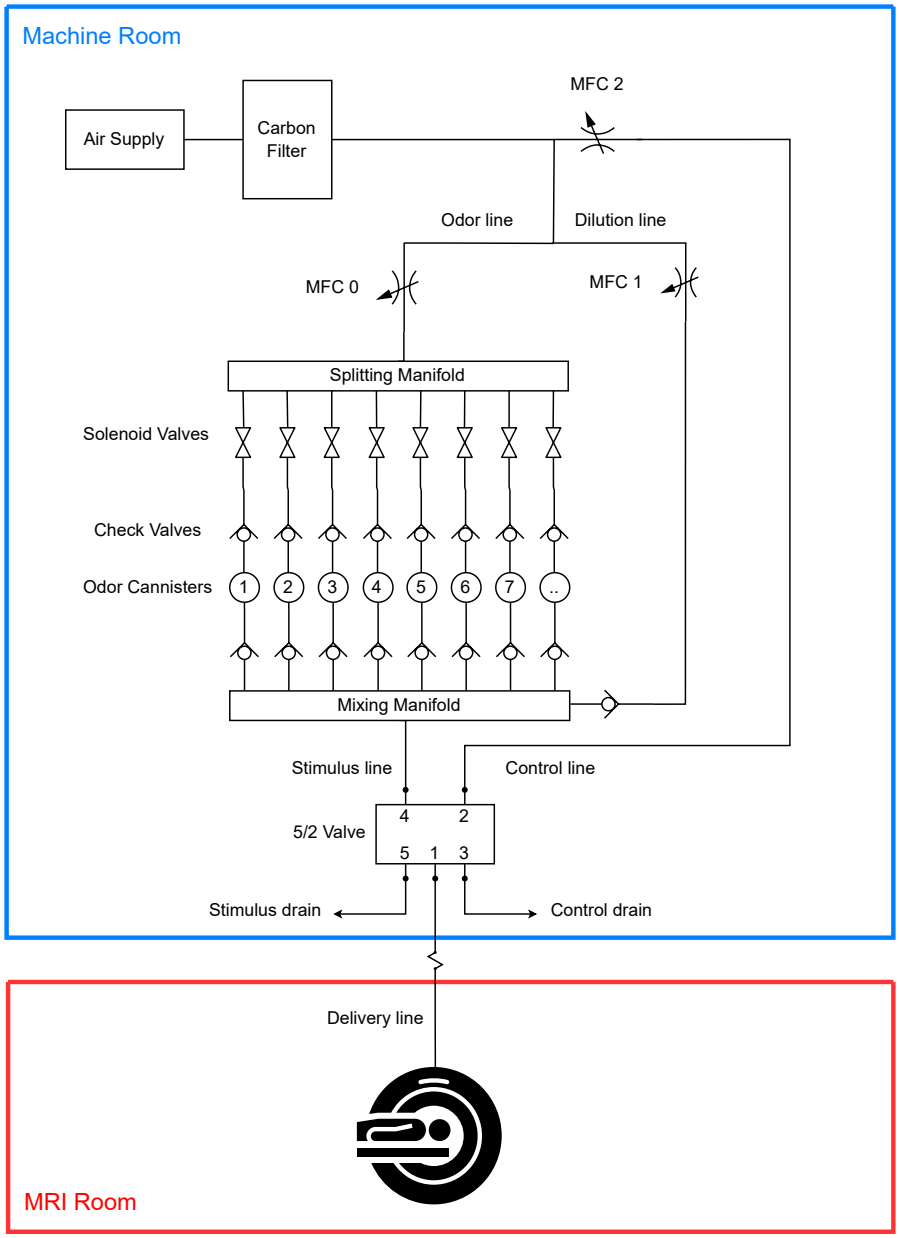

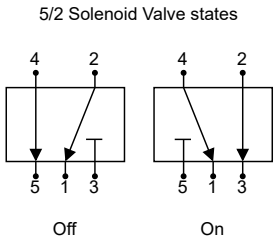

A possible method to reduce the cross-contamination in the Lorig design is proposed by adding a third control line, similar to the vacuum-switch configuration. This line connects to a 5/2 solenoid valve positioned after the mixing manifold. The stimulus line is connected to the other input of the valve. When the valve is off, the control line (2) will be connected to the delivery line (1) and the stimulus line (4) is connected to the stimulus drain (5). When the valve is switched on, the stimulus line (4) will be connected to the delivery line (1) and the control line (2) to the control drain (3). With this system it is possible to flush the mixing manifold with clean air from the dilution line, without delivering this flushed air to the subject. The flushed air will instead be drained through the stimulus drain, while clean air from the control line is delivered to the subject. This setup could provide an alternative to the tested Lorig setup with reduced cross-contamination.